Mon. Not. R. Astron. Soc. **000**, 1–20 (2005) Printed 2 February 2008 (MN LATEX style file v2.2)

Modelling the chromosphere and transition region of ϵ Eri (K2 V)

S. A. Sim[1,2⋆], C. Jordan[2]
[1]*Astrophysics Group, Imperial College London, Blackett Laboratory, Prince Consort Road, London, SW7 2AZ, UK*
[2]*Department of Physics (The Rudolf Peierls Centre for Theoretical Physics), University of Oxford, 1 Keble Road, OX1 3NP, UK*

arXiv:astro-ph/0506060v1 2 Jun 2005

2 February 2008

ABSTRACT

Measurements of ultraviolet line fluxes from Space Telescope Imaging Spectrograph and *Far-Ultraviolet Spectroscopic Explorer* spectra of the K2-dwarf ϵ Eri are reported. These are used to develop new emission measure distributions and semi-empirical atmospheric models for the chromosphere and lower transition region of the star. These models are the most detailed constructed to date for a main-sequence star other than the Sun. New ionisation balance calculations, which account for the effect of finite density on dielectronic recombination rates, are presented for carbon, nitrogen, oxygen and silicon. The results of these calculations are significantly different from the standard Arnaud & Rothenflug ion balance, particularly for alkali-like ions. The new atmospheric models are used to place constraints on possible First Ionisation Potential (FIP) related abundance variations in the lower atmosphere and to discuss limitations of single-component models for the interpretation of certain optically thick line fluxes.

Key words: radiative transfer - stars: chromospheres - stars: individual (ϵ Eridani) - stars: late-type

1 INTRODUCTION

Although it has long been known that cool main-sequence stars have hot outer atmospheres the question of how these regions are heated remains unanswered. This is, in part, due to the complexity of stellar atmospheres arising from the interplay of sub-photospheric convection, rotation and magnetic fields – in order to distinguish between different physical processes quantitative analyses and models are required.

Atmospheric models fall into two broad categories, those which are constructed from theory (e.g. those developed by Fontenla, Avrett & Loeser 1993, 2002 or Cuntz et al. 1999) and those which are constructed semi-empirically, based on a combination of observations and a few elementary physical assumptions (e.g. the Vernazza, Avrett & Loeser 1973, 1976, 1981 solar models). Semi-empirical models are vital since it is only by comparison with properties deduced from observations that theoretical models can be tested.

In this paper new semi-empirical models are developed for the chromosphere and lower transition region of the K2-dwarf ϵ Eri. This complements our recent studies of the outer atmosphere in which the mean electron pressure was measured (Jordan et al. 2001a); line widths were measured and used to investigate the non-thermal velocity fields within the atmosphere and place constraints upon the possibility of coronal heating by wave dissipation (Sim & Jordan 2003a); and emission measure distributions were used to derive new information about the area occupied by emitting material in the upper transition region (Sim & Jordan 2003b).

Previously, semi-empirical models have been constructed for ϵ Eri by Kelch (1978), Simon, Kelch & Linsky (1980) and Thatcher, Robinson & Rees (1991). The Kelch (1978) model was based on observations of the Ca II and Mg II resonance lines and described the upper photosphere and chromosphere (extending to an electron temperature $\log T_e[\mathrm{K}] = 4.3$). Simon et al. (1980) used ultraviolet observations of Si II, Si III and C II recorded with the *International Ultraviolet Explorer* (*IUE*) to develop the upper parts of the Kelch (1978) model. Their model extends to $\log T_e[\mathrm{K}] = 4.7$. Thatcher et al. (1991) used infrared lines of Ca II, the Na D doublet and lines from the H Balmer series to further develop the chromospheric part of the Kelch (1978) model and extended the model to $\log T_e[\mathrm{K}] = 5.6$.

The new models presented here are based on ultraviolet observations made with the Space Telescope Imaging Spectrograph (STIS) on board the *Hubble Space Telescope* and with the *Far-Ultraviolet Spectroscopic Explorer* (*FUSE*) satellite (see Section 2). The high signal-to-noise ratio, high spectral resolution and large combined spectral coverage of these data are ideal for quantitative modelling; they provide much tighter constraints on the model than did the *IUE* data and allow much more robust conclusions to be drawn. In particular, the improved measurements of the transition region pressure, together with radiative transfer calculations, lead to more reliable models from the photosphere to the transition region.

An important limitation of the available spectroscopic data is that, in common with all such observations of main-sequence stars

⋆ s.sim@imperial.ac.uk

other than the Sun, they contain no direct information on the spatial inhomogeneities (because the source is unresolved). Although we have been able to deduce information about the inhomogeneity in the upper transition region (Sim & Jordan 2003b), the same method cannot yet be applied to the deeper parts of the atmosphere since the local means of energy deposition is not understood. Here, for the most part, the simplest assumption, that of homogeneity, is made – thus the models are representative of the "average" atmosphere. Although the interpretation of "average" models requires considerable care, they are extremely important since they contain the most information that can be extracted directly from the data alone and theoretical models must be consistent with the mean properties. Two-component theoretical models of a K2 V star chromosphere have been made by Cuntz et al. (1999), using empirical relations between the area covered by magnetic fields and stellar rotation periods. We also derive a two-component by applying the emitting area that we found at 10^5 K (Sim & Jordan 2003b) as an upper limit to regions at lower temperatures – solar observations show that the area occupied by supergranulation cells remains constant between $\sim 2 \times 10^4$ K and 10^5 K, before decreasing in the chromosphere.

Another limitation to the modelling is the accuracy of the atomic data used – for many of the measured line fluxes, the observational uncertainty is small compared to possible errors in the atomic rates. In particular, the standard sets of ionisation balance calculations used for transition region lines are inadequate for modelling to the precision of the STIS data. In this paper a new ionisation balance calculation is presented in which rates that account for variations in the dielectronic recombination rate with density are used; although not definitive, this calculation highlights the need for further work on recombination rates at non-zero density.

The ultraviolet observations and measurements of the emission line fluxes are discussed in Section 2. In Section 3 the new ionisation balance calculations are discussed. They are used in the construction of emission measure distributions (EMDs) in Section 4. A preliminary single-component atmospheric model is developed in Section 5 and improvements to this model are discussed in Section 6. In Section 7, the simple two-component model is presented and conclusions are drawn in Section 8.

2 OBSERVATIONS

2.1 Flux measurements

The models developed are based on measurements of fluxes for a variety of emission lines in STIS and *FUSE* spectra of ϵ Eri. Table 1 gives the measured fluxes for lines in the STIS spectra (see Jordan et al. 2001b for details of our STIS spectra). These were obtained by direct integration across line profiles and, where possible, by performing single-Gaussian fits. (The line widths and shifts deduced from Gaussian fits have been published elsewhere: Sim & Jordan 2003a.) The errors given are tolerances based on the signal-to-noise, the uncertainty in the background level and, where applicable, the goodness of the Gaussian fits. Four of the lines listed in Table 1 are affected by blending. Three of these (O IV 1404.8 Å, Si II 2335.3 Å and S IV 1404.8 Å) have been discussed by Jordan et al. (2001a). The other, Si II 1260.4 Å, is suspected to be a close blend with C I 1260.6 Å. The Al III $^2S_{1/2} - {}^2P_{1/2}$ line at 1862.8 Å it too weak to measure. This suggests that the Al III 1854.7-Å line is also blended, probably with an iron line. (In the optically thin limit the Al III 1854.7-Å line should have double the flux of the 1862.8-Å line, but the observed 1854.7-Å feature is more than twice as strong as that at 1862.8 Å.)

It is noteworthy that when the *IUE* fluxes reported for ϵ Eri by Jordan et al. (1987) are compared with the new fluxes from STIS there is no evidence of significant differences. Since the *IUE* and STIS data were recorded seventeen years apart this argues against significant long term variability in the atmosphere.

The STIS fluxes are supplemented by measurements from *FUSE* spectra of ϵ Eri. The *FUSE* observations are discussed by Redfield et al. (2002). The lines in the *FUSE* spectrum that are used here, and our measurements of their fluxes, are listed in Table 2. As for the STIS measurements, the fluxes were obtained by a combination of direct integration and single-Gaussian fits. The *FUSE* instrument has four channels which record spectra, 1-LiF, 2-LiF, 1-SiC and 2-Sic. Most of the *FUSE* line fluxes have been measured from spectra recorded with the 1-LiF channel (this channel is used to guide the *FUSE* line-of-sight). Unfortunately, the S VI 933.4-Å, C III 977.0-Å and H I 972.5-Å lines do not fall in the 1-LiF spectra. Therefore, the fluxes for these lines have been measured from 1-SiC spectra which are susceptible to losing photons due to channel drift (Sankrit et al. 2001). Measurements of the strong O VI line fluxes (which occur in both the 1-LiF and 1-SiC spectra) were used to correct the 1-SiC line fluxes for channel drift but the measurement uncertainties are still largest for the 1-SiC measurements.

Redfield et al. (2002) have published independent measurements of these line fluxes in the ϵ Eri spectrum. In almost every case, the fluxes here agree with those given by Redfield et al. (2002) to within the quoted errors. The only exception is the C III 1175-Å multiplet; in this case, Redfield et al. (2002) report a flux which is smaller by ~ 20 per cent than that found here, while the errors are only ~ 10 per cent. It is noted that their fit (their fig. 10) does appear to underestimate the peak fluxes in this multiplet. However, this difference is not significant given the other sources of uncertainty in the modelling. The total C III 1175-Å flux measured from STIS (Table 1) and that derived from *FUSE* (Table 2) are very similar (they agree to within the measurement uncertainties). This argues against short term variations in the emission line fluxes since the STIS and *FUSE* data were recorded nine months apart.

2.2 Interstellar absorption

Interstellar absorption can be clearly identified in the line profiles of several of the resonance lines. This is important since it allows information to be derived about the local interstellar medium (see, for example, Wood et al. 2000 or Redfield & Linsky 2002 for such studies involving spectra of ϵ Eri) but also because it must be taken into consideration when analysing the spectrum of the star. The largest effect is in lines of the H I Lyman series (this H I absorption has been studied by Dring et al. (1997) who used it to determine the interstellar H I and D I column densities). However, there is also significant absorption in the Mg II h and k lines and several transitions involving the ground states of C II and Si II. The C II and Si II lines affected are listed in Table 3 which also gives estimated line centre opacities (τ_0) for interstellar absorption in each line. These have been computed with the C/H abundance for the interstellar medium given by Cardelli et al. (1996) (gas phase C/H ratio of 1.4×10^{-4}) and assuming a solar photospheric value for the relative Si/C abundance (Grevesse & Sauval 1998). The interstellar H I column density was taken from Dring et al. (1997) and the interstellar line width parameter was estimated from the observed interstellar absorption in the Mg II lines. For the calculations of

Table 1. Emission line fluxes measured from the ϵ Eri *STIS* spectra. λ_0 is the rest wavelength. "bl." indicates that the line is part of a blend: in such cases the *total* measured flux in the blend is given as an upper limit to the line flux. The rest wavelengths are taken from Griesmann & Kling (2000) [C IV and Si IV], Kaufman & Martin (1993) [S IV] and Kurucz & Bell (1995) [all other lines].

Ion	Transition	λ_0 (Å)	Flux at Earth (10^{-13} ergs cm^{-2} s^{-1})
H I	$1s\ ^2S - 2p\ ^2P$	1215.671	160 ± 1
C II	$2s^22p\ ^2P_{1/2} - 2s2p^2\ ^2D_{3/2}$	1334.532	1.88 ± 0.06
C II	$2s^22p\ ^2P_{3/2} - 2s2p^2\ ^2D_{5/2,3/2}$	1335.68 bl.	4.84 ± 0.10
C III	$2s2p\ ^3P_1 - 2p^2\ ^3P_2$	1174.933	0.41 ± 0.06
C III	$2s2p\ ^3P_0 - 2p^2\ ^3P_1$	1175.263	0.41 ± 0.06
C III	$2s2p\ ^3P_{2,1} - 2p^2\ ^3P_{2,1}$	1175.69 bl.	1.49 ± 0.06
C III	$2s2p\ ^3P_1 - 2p^2\ ^3P_0$	1175.987	0.41 ± 0.06
C III	$2s2p\ ^3P_2 - 2p^2\ ^3P_1$	1176.370	0.46 ± 0.06
C IV	$2s\ ^2S_{1/2} - 2p\ ^2P_{3/2}$	1548.204	5.59 ± 0.11
C IV	$2s\ ^2S_{1/2} - 2p\ ^2P_{1/2}$	1550.781	2.82 ± 0.07
N IV	$2s^2\ ^1S_0 - 2s2p\ ^3P_1$	1486.496	0.045 ± 0.015
N V	$2s\ ^2S_{1/2} - 2p\ ^2P_{3/2}$	1238.821	0.94 ± 0.03
N V	$2s\ ^2S_{1/2} - 2p\ ^2P_{1/2}$	1242.804	0.46 ± 0.02
O III	$2s^22p^2\ ^3P_1 - 2s2p^3\ ^5S_2$	1660.809	0.058 ± 0.015
O III	$2s^22p^2\ ^3P_2 - 2s2p^3\ ^5S_2$	1666.150	0.121 ± 0.015
O IV	$2s^22p\ ^2P_{1/2} - 2s2p^2\ ^4P_{1/2}$	1399.780	0.054 ± 0.005
O IV	$2s^22p\ ^2P_{3/2} - 2s2p^2\ ^4P_{5/2}$	1401.157	0.181 ± 0.005
O IV	$2s^22p\ ^2P_{3/2} - 2s2p^2\ ^4P_{3/2}$	1404.806	0.069 ± 0.005 bl.
O IV	$2s^22p\ ^2P_{3/2} - 2s2p^2\ ^4P_{1/2}$	1407.382	0.052 ± 0.005
O V	$2s^2\ ^1S_0 - 2s2p\ ^3P_1$	1218.344	0.68 ± 0.04
O V	$2s2p\ ^1P_1 - 2p^2\ ^1D_2$	1371.296	0.105 ± 0.005
Mg II	$3s\ ^2S_{1/2} - 3p\ ^2P_{3/2}$	2796.352	305 ± 6
Mg II	$3s\ ^2S_{1/2} - 3p\ ^2P_{1/2}$	2803.531	232 ± 5
Al III	$3s\ ^2S_{1/2} - 3p\ ^2P_{3/2}$	1854.716	0.51 ± 0.06 bl?
Si II	$3s^23p\ ^2P_{1/2} - 3s3p^2\ ^2P_{3/2}$	1190.416	0.10 ± 0.03
Si II	$3s^23p\ ^2P_{1/2} - 3s3p^2\ ^2P_{1/2}$	1193.290	0.09 ± 0.04
Si II	$3s^23p\ ^2P_{3/2} - 3s3p^2\ ^2P_{3/2}$	1194.500	0.18 ± 0.03
Si II	$3s^23p\ ^2P_{3/2} - 3s3p^2\ ^2P_{1/2}$	1197.394	0.10 ± 0.04
Si II	$3p\ ^2P_{1/2} - 3d\ ^2D_{3/2}$	1260.422	0.191 ± 0.03 bl.
Si II	$3p\ ^2P_{3/2} - 3d\ ^2D_{5/2}$	1264.738	0.505 ± 0.05
Si II	$3p\ ^2P_{3/2} - 3d\ ^2D_{3/2}$	1265.002	0.172 ± 0.03
Si II	$3s^23p\ ^2P_{1/2} - 3s3p^2\ ^2S_{1/2}$	1304.370	0.133 ± 0.008
Si II	$3s^23p\ ^2P_{3/2} - 3s3p^2\ ^2S_{1/2}$	1309.276	0.222 ± 0.010
Si II	$3p\ ^2P_{1/2} - 4s\ ^2S_{1/2}$	1526.707	0.508 ± 0.005
Si II	$3p\ ^2P_{3/2} - 4s\ ^2S_{1/2}$	1533.431	0.607 ± 0.005
Si II	$3s^23p\ ^2P_{1/2} - 3s3p^2\ ^2D_{3/2}$	1808.013	6.39 ± 0.06
Si II	$3s^23p\ ^2P_{3/2} - 3s3p^2\ ^2D_{5/2}$	1816.928	10.42 ± 0.07
Si II	$3s^23p\ ^2P_{3/2} - 3s3p^2\ ^2D_{3/2}$	1817.451	3.20 ± 0.06
Si II	$3s^23p\ ^2P_{1/2} - 3s3p^2\ ^4P_{1/2}$	2335.123	3.31 ± 0.07
Si II	$3s^23p\ ^2P_{3/2} - 3s3p^2\ ^4P_{5/2}$	2335.321	2.23 ± 0.07 bl.
Si II	$3s^23p\ ^2P_{3/2} - 3s3p^2\ ^4P_{1/2}$	2350.891	3.04 ± 0.07
Si III	$3s^2\ ^1S_0 - 3s3p\ ^1P_1$	1206.500	3.60 ± 0.10
Si III	$3s3p\ ^3P_1 - 3p^2\ ^3P_2$	1294.545	0.052 ± 0.005
Si III	$3s3p\ ^3P_0 - 3p^2\ ^3P_1$	1296.726	0.041 ± 0.005
Si III	$3s3p\ ^3P_{2,1} - 3p^2\ ^3P_{2,1}$	1298.93 bl.	0.167 ± 0.005
Si III	$3s3p\ ^3P_1 - 3p^2\ ^3P_0$	1301.149	0.028 ± 0.005
Si III	$3s3p\ ^3P_2 - 3p^2\ ^3P_1$	1303.323	0.062 ± 0.005
Si III	$3s^2\ ^1S_0 - 3s3p\ ^3P_1$	1892.030	1.25 ± 0.05
Si IV	$3s\ ^2S_{1/2} - 3p\ ^2P_{3/2}$	1393.760	2.30 ± 0.06
Si IV	$3s\ ^2S_{1/2} - 3p\ ^2P_{1/2}$	1402.773	1.21 ± 0.05
S II	$3s^23p^3\ ^4S_{3/2} - 3s3p^4\ ^4P_{1/2}$	1250.584	0.029 ± 0.010
S II	$3s^23p^3\ ^4S_{3/2} - 3s3p^4\ ^4P_{3/2}$	1253.811	0.066 ± 0.005
S II	$3s^23p^3\ ^4S_{3/2} - 3s3p^4\ ^4P_{5/2}$	1259.519	0.099 ± 0.005
S IV	$3s^23p\ ^2P_{1/2} - 3s3p^2\ ^4P_{1/2}$	1404.808	0.069 ± 0.005 bl.
S IV	$3s^23p\ ^2P_{3/2} - 3s3p^2\ ^4P_{5/2}$	1406.016	0.032 ± 0.007
S IV	$3s^23p\ ^2P_{3/2} - 3s3p^2\ ^4P_{3/2}$	1416.887	0.042 ± 0.007
Cl I	$3p^5\ ^2P_{1/2} - 3p^4(^3P)4s\ ^2P_{1/2}$	1351.656	0.198 ± 0.005

Table 2. Fluxes for emission lines in the ϵ Eri *FUSE* spectra. Unless otherwise indicated, all lines were measured in the 1-LiF spectra. λ_0 is the rest wavelength. The rest wavelengths are taken from Kurucz & Bell (1995).

Ion	Transition	λ_0 (Å)	Flux at Earth (10^{-13} ergs cm^{-2} s^{-1})
H I[a]	$1s\ ^2S - 4p\ ^2P$	972.537	0.63 ± 0.08
H I	$1s\ ^2S - 3p\ ^2P$	1025.722	3.66 ± 0.12
C II	$2s2p^2\ ^4P_{1/2} - 2p^3\ ^4S_{3/2}$	1009.858	0.012 ± 0.007
C II	$2s2p^2\ ^4P_{3/2} - 2p^3\ ^4S_{3/2}$	1010.083	0.027 ± 0.007
C II	$2s2p^2\ ^4P_{5/2} - 2p^3\ ^4S_{3/2}$	1010.371	0.046 ± 0.007
C II	$2s^22p\ ^2P_{1/2} - 2s2p^2\ ^2S_{1/2}$	1036.337	0.120 ± 0.014
C II	$2s^22p\ ^2P_{3/2} - 2s2p^2\ ^2S_{1/2}$	1037.018	0.291 ± 0.008
C III[a]	$2s^2\ ^1S_0 - 2s2p\ ^1P_1$	977.020	4.67 ± 0.10
C III	$2s2p\ ^3P_1 - 2p^2\ ^3P_2$	1174.933	0.435 ± 0.015
C III	$2s2p\ ^3P_0 - 2p^2\ ^3P_1$	1175.263	0.425 ± 0.015
C III	$2s2p\ ^3P_{2,1} - 2p^2\ ^3P_{2,1}$	1175.63 bl.	1.519 ± 0.015
C III	$2s2p\ ^3P_1 - 2p^2\ ^3P_0$	1175.987	0.405 ± 0.015
C III	$2s2p\ ^3P_2 - 2p^2\ ^3P_1$	1176.370	0.467 ± 0.015
N III	$2s^22p\ ^2P_{3/2} - 2s2p^2\ ^2D_{3/2,5/2}$	991.54 bl.	0.33 ± 0.08
O VI	$2s\ ^2S_{1/2} - 2p\ ^2P_{3/2}$	1031.912	4.59 ± 0.16
O VI	$2s\ ^2S_{1/2} - 2p\ ^2P_{1/2}$	1037.613	2.26 ± 0.08
Si III	$3s3p\ ^3P_0 - 3s3d\ ^3D_1$	1108.358	0.020 ± 0.020
Si III	$3s3p\ ^3P_1 - 3s3d\ ^3D_{1,2}$	1109.96 bl.	0.065 ± 0.020
Si III	$3s3p\ ^3P_2 - 3s3d\ ^3D_{1,2,3}$	1113.20 bl.	0.121 ± 0.020
S IV	$3s^23p\ ^2P_{1/2} - 3s3p^2\ ^2D_{3/2}$	1062.678	0.038 ± 0.020
S IV	$3s^23p\ ^2P_{3/2} - 3s3p^2\ ^2D_{5/2}$	1072.996	0.056 ± 0.020
S VI[a]	$3s\ ^2S_{1/2} - 3p\ ^2P_{3/2}$	933.378	0.24 ± 0.08

[a] Measured from 1-SiC spectra.

Table 3. Lines of C II and Si II affected by interstellar absorption and their calculated interstellar line centre opacities (τ_0) The absolute values of τ_0 are uncertain but the relative values are reliable (see text).

Ion	λ_0 (Å)	τ_0
C II	1334.5	5.6
C II	1036.3	4.4
Si II	1190.4	1.7
Si II	1193.3	3.5
Si II	1260.4	7.5
Si II	1304.4	0.2
Si II	1526.7	1.0
Si II	1808.0	2×10^{-2}

τ_0, it has been assumed that all the interstellar C and Si is singly ionised – thus the listed values are upper limits.

The relative values of τ_0 suggest that the 1260.4-Å line should show the greatest interstellar absorption of the Si II lines and that there should be very little effect on the 1526.7, 1304.4 or 1808.0-Å lines. This is consistent with the observed line profiles – of the Si II lines, only the 1260.4-Å transition shows evidence of self-reversal (in addition to line blending). The C II resonance lines at 1334.5 Å (observed with STIS) and 1036.3 Å (observed with *FUSE*) are expected to have similar optical depths due to interstellar absorption and both show evidence of absorption.

3 IONISATION BALANCE CALCULATIONS

Ionization equilibrium populations are needed for quantitative analyses of stellar atmospheres. Above the chromosphere, for most ions the dominant ionisation processes are collisional; either direct collisional ionisation or collisional excitation followed by autoionisation (Goldberg, Dupree & Allen 1965). Photoionisation is usually not important. Both radiative recombination and dielectronic recombination (Burgess 1964) must be included. Currently, the most widely used ionisation balance calculations in the literature are those of Arnaud & Rothenflug (1985) and Mazzotta et al. (1998) or, for ions of iron, those by Arnaud & Raymond (1992). More recently high precision calculations have been made for specific elements or ions (e.g. Nahar 1995 [Si I]; Nahar 1996 [Si II]; Nahar & Pradhan 1997 [C and N]; Nahar 1999 [O]; Nahar, Pradhan & Zhang 2000 [C, including relativistic effects]). In common with the earlier work (Arnaud & Rothenflug 1985), usually only the zero-density limit is considered for recombination rates.

Burgess (1965) pointed out that non-zero density reduces the dielectronic recombination rate because highly excited states effectively become part of the continuum. Jordan (1969a) attempted to account for this in an approximate way in her ionisation balance calculations and Judge et al. (1995) used recombination rates corrected for finite density (based on calculations by Summers 1974a,b) in their analysis of solar data, but none of the more recent calculations mentioned above address this issue. The effects are significant for ϵ Eri, where the transition region pressure (and therefore density) is higher than in the Sun – a reduction of the dielectronic recombination rate will alter the ionisation balance, affecting, in particular, the important Li-like and Na-like ions (the sensitivity of these ions is apparent from the calculations of Jordan 1969a). It is well known from solar work that emission measures derived from Li-like and Na-like ions often appear anomalous (Burton et al. 1971, Dupree 1972, Judge et al. 1995). It has also been noted in analyses of other cool stars (e.g. Jordan et al. 1987). Similar results are found for ϵ Eri; if the standard Arnaud & Rothenflug (1985) ionisation balance calculations are adopted, the loci of Li-like and Na-like ions tend to lie too high compared with those of other ions (see Section 4). In view of the sensitivity of these ions

to the density-dependent reduction to the recombination rates it is necessary to attempt to include this effect in the ionisation balance.

Summers (1972, 1974a,b) computed recombination rates as a function of both temperature and electron density (N_e) for various elements, including those of primary interest here (C, N, O, Si). Rates computed at electron densities of $\log N_e[\mathrm{cm}^{-3}] = 8.0$ and 12 were taken from Summers (1974b). For C, N, O and Si these rates were extrapolated linearly against temperature in log-log space to find recombination rates appropriate for the mean transition region pressure in ϵ Eri ($\log P_e[\mathrm{cm}^{-3}\ \mathrm{K}] = 15.68$, Jordan et al. 2001a). The recombination rates determined in this way for several important ions (C IV, N V and Si IV) are different by several hundred percent from the zero-density limit; this is sufficiently large to noticeably affect the ionisation balance.

These extrapolated recombination rates were used together with collisional ionisation rates from Bell et al. (1983) to compute the fractional ion populations as a function of temperature for C II – IV, N III – V, O III – O VI and Si II – IV. Photoionisation has been neglected for these calculations, as has charge exchange for the C, N and O ions. Charge exchange (with rates taken from Arnaud & Rothenflug 1985) was included for Si. As expected, the ionisation fractions computed differ most significantly from those of Arnaud & Rothenflug (1985) for Li-like and Na-like ion, but there are also differences for several lower ionisation stages. The reduction in recombination rates causes the peak ionisation fraction to occur at lower temperatures for many ions (as apparent in Jordan 1969a).

These effects are illustrated in Fig. 1 which shows ionisation balance calculations for C. Two sets of zero-density calculations are shown (Arnaud & Rothenflug 1985; Nahar & Pradhan 1997) along with Jordan's (1969a) results for a solar pressure and the new computations for ϵ Eri. Generally, the zero-density calculations (Arnaud & Rothenflug 1985 and Nahar & Pradhan 1997) agree well with each other but there are significant differences from the finite density cases. The agreement between the new calculations and those of Jordan (1969a) is good – although Jordan's calculations were intended for densities in the quiet Sun, she found later that the density sensitivity was overestimated and that the results are more applicable to higher pressures such as those found in active regions, or ϵ Eri. The results for the other elements considered (N, O, Si) are all similar. The largest differences between the new calculations and those by Jordan (1969a) are for Si since the latter did not include charge exchange processes.

The new ionisation balance calculations for C, N, O and Si are used in the emission measure modelling (see Section 4) and the recombination rates computed for finite density are employed in the atomic models of Si and C discussed in Section 5.2. The computed ionisation fractions are tabulated in Appendix A. The accuracy of these ion fractions is limited by the accuracy of the Summers (1972,1974a,b) recombination rates; there is now a real need for modern calculations of di-electronic recombination rates at finite density.

4 EMISSION MEASURE DISTRIBUTION (EMD)

4.1 Emission measure loci

In this section the fluxes presented in Section 2 are used to construct loci which constrain the mean emission measure distribution $Em^{0.3}(T_e)$. The principles of this method have been discussed at length elsewhere (e.g. Jordan & Brown 1981). The notation and definitions used by Sim & Jordan (2003b) are adopted here.

The standard method of constructing emission measure loci from line fluxes is only valid for optically thin lines. For optically thick lines radiative transfer calculations are required. In order to construct a "first-cut" model, however, even optically thick lines can be included in the emission measure analysis by assuming that they are part of a multiplet which is effectively optically thin. For lines in which scattering is the only opacity source this assumption should not lead to errors of more than a factor of two. This approach is used in this section. In Section 5, full radiative transfer calculations are discussed and used to improve the calculations presented here.

Throughout the following discussion, solar photospheric values have been adopted for the relative abundances of the elements (from Grevesse & Sauval 1998), with absolute values scaled to the ϵ Eri metallicity derived by Drake & Smith (1993). The observed line fluxes have been converted to fluxes at the stellar surface using the stellar parameters adopted by Jordan et al. (2001b, table 1). We investigate later the differences which result from adopting the recent solar abundances derived by Asplund, Grevesse & Sauval (2004).

4.2 Density-insensitive STIS lines

For many of the strong emission lines in the STIS wavelength range, the contribution function $K(T_e)$[1] is almost completely insensitive to the density. This generally occurs for permitted transition in which the upper level is predominantly excited by collisions from the ground state. Such lines place the strongest constraints on the EMD since their loci are independent of any uncertainty in the electron pressure.

Table 4 lists the density-insensitive lines/multiplets from the STIS lines (the insensitivity criterion was taken to be a variation in $K(T_e)$ of less than ten per cent resulting from a variation of $\log P_e$ by ± 0.3 dex around the mean transition region pressure). Table 4 also indicates whether the lines may reasonably be assumed to be optically thin or whether only the multiplet as a whole is likely to be thin (it is stressed that optically thick lines are treated with radiative transfer calculations at a later stage, see Section 5).

The multiplets listed in Table 4 have been used to construct emission measure loci. The $K(T_e)$ contribution functions were computed with the CHIANTI database (v3.03; Dere at al. 1997; Dere et al. 2001). For C, N, O and Si the ionisation fractions were computed as described in Section 3. For other elements the Arnaud & Rothenflug (1985) ionisation fractions were adopted. The loci computed are plotted in Fig. 2.

The loci suggest a smooth EMD decreasing from the chromosphere to a minimum somewhere in the mid-transition region at around $\log T_e \approx 5.3$. There is a sufficiently large number of lines to provide temperature coverage throughout this part of the atmosphere, placing constraints on the EMD that are at least as complete as those for the Sun.

The lightly drawn loci in Fig. 2 (offset by +3 dex for clarity) show the constraints derived from the same line fluxes if the Arnaud & Rothenflug (1985) ionisation calculations are used for every ion. In this case, C IV and Si IV are clearly anomalous by factors > 2 and N V also appears to lie rather high. However, when the new ionisation calculations are adopted (Section 3) the loci from these

[1] An explicit expression for the contribution function ($K(T_e)$) in terms of abundance, ionisation fraction, degree of excitation, electron number density and Einstein-A coefficient is given by Sim & Jordan (2003b).

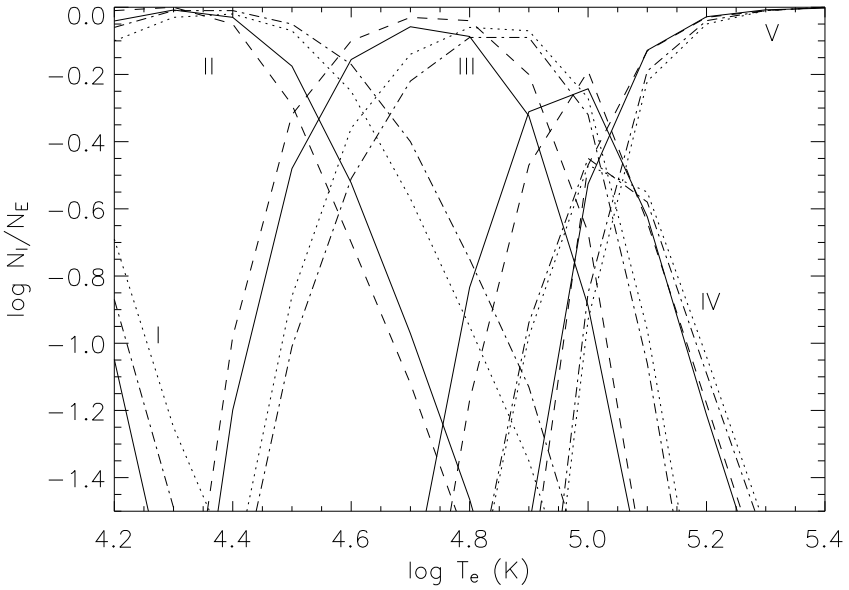

Figure 1. Ionisation fractions for C ($N_{\rm I}/N_{\rm E}$) as a function of temperature. C I – C V are shown, although only results for C II – C IV are needed in Section 4. The curves are labelled with the ionisation stage they represent. The solid curves are the ionisation fractions computed here. The dashed curves are the finite density calculations of Jordan (1969a); the dotted curves are the Nahar & Pradhan (1997) ion fractions and the dot-dash curves are from Arnaud & Rothenflug (1985).

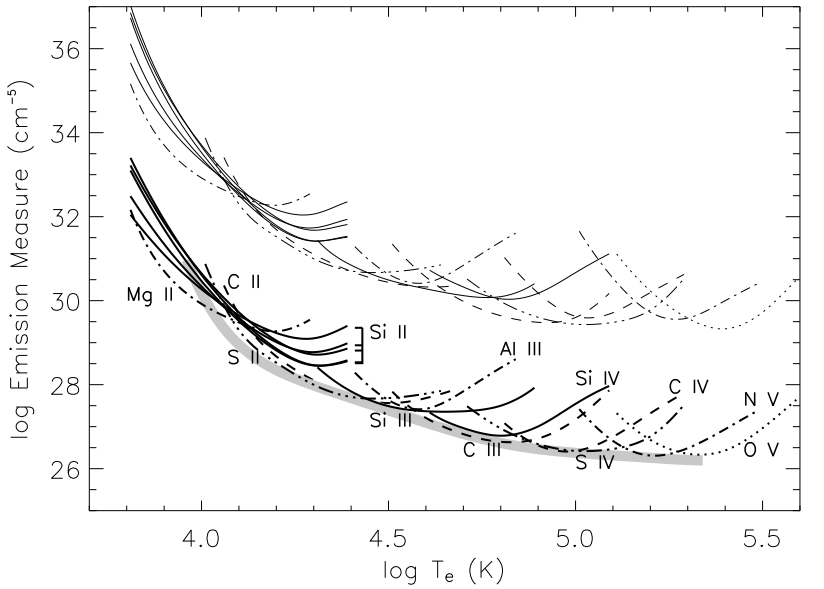

Figure 2. Emission measure loci from density-insensitive lines in the ϵ Eri STIS spectrum. The solid curves are for lines of Si; the dashed curves for C; the dotted curve for O; dot-dash curves are used for N, Al and Mg; and the triple-dot-dash curves are for S. The heavy lines show the loci computed using the new ionisation fractions from Section 3 and are labelled with the ion they represent. The light lines show the loci computed if all ion fractions are taken from Arnaud & Rothenflug. These curves have been off-set by +3 dex, for clarity. The broad, light curve is the mean EMD corresponding to DEMD-A (see Section 4.5).

Table 4. Density-insensitive lines used for emission measure modelling. Where an entry is given in parenthesis it is likely that the lines are affected by radiative transfer effects which are dealt with in Section 5.

Ion	λ (Å)	Assumed opacity
(C II	1335	multiplet effectively thin)
C III	1175	thin
C IV	1550	thin
N V	1240	thin
O V	1371	thin
(Mg II	2800	multiplet effectively thin)
Al III	1854	effectively thin
Si II	1810	multiplet effectively thin
Si II	1530	multiplet effectively thin
Si II	1308	multiplet effectively thin
Si II	1260	multiplet effectively thin
Si II	1195	multiplet effectively thin
Si III	1206	effectively thin
Si IV	1400	thin
S II	1255	multiplet effectively thin
S IV	1406	thin

Li-like and Na-like ions are in much better agreement with those of other ions. The agreement is still not perfect, in particular the Si IV locus still lies higher than that of C III by about 30 per cent, but this difference is small compared to the likely residual uncertainty in the ionisation balance calculations. The Al III locus is also rather high; although this may be the result of blending in the observed Al III line, it may also be the result of errors in the ionisation balance; like C IV, Al III is an alkali but no new ionisation calculations have been performed for this ion.

It is concluded that all the loci which appear significantly anomalous when the Arnaud & Rothenflug (1985) ionisation balance calculations are adopted are likely to be the result of errors in the recombination rates used in that ionisation balance, owing to the density dependence of dielectronic recombination. This is in contrast to the analysis of solar data by Judge et al. (1995); they find that loci derived for alkali-like ions are still discordant, even if they account for the density-sensitivity of dielectronic recombination and they interpret this as evidence of dynamic or diffusive effects (although they do state that uncertainties in the recombination rates may still be significant). [2] This issue cannot be fully resolved without reliable recombination rates.

4.3 Density-sensitive STIS lines

The density-insensitive *STIS* loci can be supplemented by loci derived from density-sensitive lines/multiplets. Table 5 lists the density-sensitive multiplets from the STIS data. Most of these multiplets and the associated atomic data have been discussed by Jordan et al. (2001a) where they were used to deduce the mean transition region pressure. The Si II 2334-Å multiplet is not used here; this multiplet is density-sensitive but there are line blends and obvious problems with the atomic data.

Table 5. Density-sensitive lines used for emission measure modelling.

Ion	λ (Å)	Opacity
N IV	1486	thin
O III	1663	thin
O IV	1400	thin
O V	1218	thin
Si III	1892	thin
Si III	1300	thin

The loci deduced from the density-sensitive loci are plotted in Fig 3. In general there is good agreement between the density-sensitive and density-insensitive loci when $\log P_e[\mathrm{cm}^{-3}\,\mathrm{K}] = 15.68$ is adopted. The N IV and, in particular, the O IV loci lie lower than those from density-insensitive lines at similar temperatures. A similar effect has been noted in the Sun; Judge & Brekke (1994) found that loci derived from density-sensitive lines lie lower than those from resonance lines by a significant factor. In part this may be due to uncertainties in the atomic data for these transitions (it is known that there are inadequacies in the O IV atomic data – see the discussion by Jordan et al. 2001a). There are also complications in the interpretation of the loci from density-sensitive multiplets resulting from inhomogeneity in the atmosphere (Judge & Brekke 1994). If the atmosphere is inhomogeneous then loci derived from density-insensitive lines will represent unbiased averages over the inhomogeneous structure. In contrast, the density-sensitive lines will form predominantly in regions with higher or lower density than average resulting in a pressure-weighted average. To investigate this effect it is necessary to quantify the nature of the sensitivity of the density-sensitive lines. Fig. 4 shows loci derived for the density-sensitive lines at different pressures. For most of the lines, a higher pressure means that less flux is formed for a given emission measure (i.e. the emission measure locus lies higher for a given flux) and vice versa. The Si III 1300-Å multiplet is an exception because of the influence of the density on the metastable ^{3}P populations. The N IV, O III and Si III 1892-Å loci are the most sensitive to errors in the pressure, changing by about 50 per cent when the pressure is varied by a factor of two. O IV and O V are interesting because, although less sensitive than O III, they respond more to a high density than a low density. Thus if there is a range of densities present in the atmosphere those places with density lower than average will not contribute significantly more than average, but those regions with high density will contribute significantly less. This may partially explain why the O IV locus appears to lie too low.

4.4 *FUSE* lines

The multiplets measured in the *FUSE* spectra provide useful supplementary constraints. Table 6 lists the multiplets observed with *FUSE* that have been used to construct emission measure loci. The loci are shown in Fig. 5.

Most of the *FUSE* loci agree well with each other, and with the STIS loci. The *FUSE* S IV locus is not consistent with the STIS loci. The S IV measurement error is large (~ 40 per cent) but not sufficient to explain the discrepancy. The most probably explanation is a systematic error in the S IV atomic data.

[2] However, Judge et al. (1995) used a mixture of lines above and below the H Lyman edge at 911 Å, whereas all the lines used here lie above 911 Å. Judge et al. (1995) rejected absorption by the Lyman continuum as a source of the discrepancies that they found, partly on the basis that centre-to-limb differences have not been observed. However, Burton et al. (1973) established the magnitude of this by observing the limb-to-disc ratio of pairs of optically thin lines from a given ion, where one was found at $\lambda > 911$ Å and the other at $\lambda < 911$ Å. This amounts to a factor of up to ~ 3 between $\lambda \sim 765$ and 835 Å. These ratios are independent of any atomic physics, abundances or intensity calibration. The effect expected for stellar observations should, of course, be less than this.

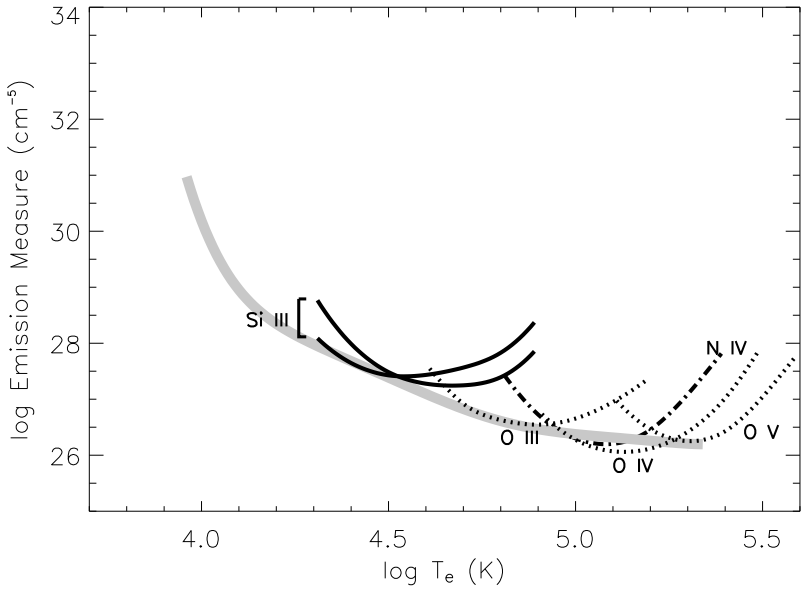

Figure 3. Emission measure loci from density-sensitive lines in the ϵ Eri STIS spectrum. The solid curves are for lines of Si; the dotted curve for O; the dot-dash curve for N. The light broad curve shows the same EMD plotted in Fig. 2.

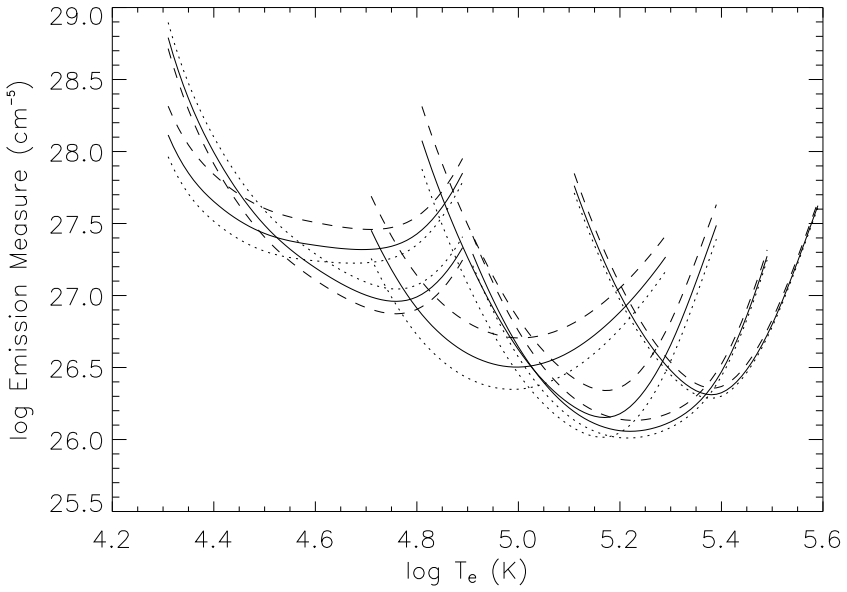

Figure 4. Emission measure loci from density-sensitive lines in the ϵ Eri *STIS* spectrum. The curves are for the same ions as indicated in Fig 3. The solid curves were calculated using the best mean electron pressure, the dotted curves using a pressure smaller than the mean by a factor of two and the dashed curves using a pressure higher than the mean by a factor of two. Note that the scale is significantly expanded compared to Figs 2 and 3.

4.5 Preliminary mean EMD

The procedure of constructing emission measure distributions from emission measure loci has come under close scrutiny in recent years (e.g. Judge, Hubeny & Brown 1997; McIntosh, Brown & Judge 1998). Since the EMD is a continuous function but we have only a finite number of constraints, each with an associated uncertainty, it is not possible to determine a unique EMD from the data alone. Thus the EMD obtained will depend on how it is obtained. However, as stressed by Judge et al. (1997), the EMD determined to be consistent with the data is still important since it represents the most information that can be extracted from the data alone, and the range of distributions that are consistent with the data is an indication of the completeness of the information provided by the data.

Here, the mean EMD ($Em^{0.3}(T_e)$) has been constructed

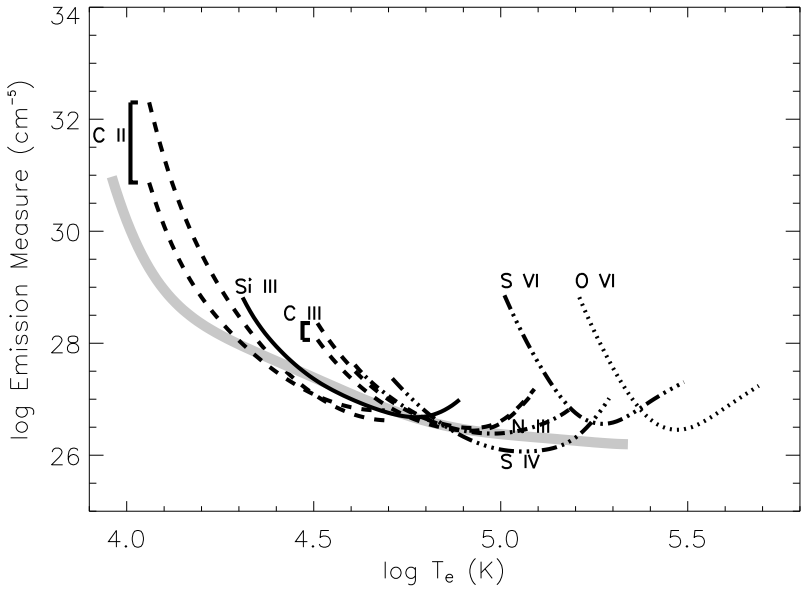

Figure 5. Emission measure loci from lines in the ϵ Eri *FUSE* spectrum. The solid curve is for the Si multiplet; the dashed curves for C; the dotted curve for O; the dot-dash curve for N; the triplet-dot-dash curves for S. The light, broad curve shows the mean EMD from Fig. 2 for comparison.

Table 6. *FUSE* lines used for emission measure modelling. The last column gives the *FUSE* channel in which the lines are observed. Only the pointing of the 1-LiF is accurate. The other channels may lose photons due to channel drift making the measurements from these channels prone to large errors.

Ion	λ (Å)	Opacity	Channel
C II	1010	effectively thin	1A-LiF
C II	1037	(effectively thin)	1A-LiF
C III	1175	thin	1B-LiF
C III	977	effectively thin	1B-SiC
N III	991	thin	1A-LiF
O VI	1035	thin	1A-LiF
Si III	1110	thin	1B-LiF
S IV	1070	thin	1A-LiF
S VI	933	thin	1B-SiC

by first obtaining the *differential emission measure distribution* (DEMD) defined by

$$\frac{\mathrm{d}Em}{\mathrm{d}\log T_e} = G(r) f(r) \frac{A(r)}{A_*(r)} N_e(T_e) N_H(T_e) \frac{\mathrm{d}r}{\mathrm{d}\log T_e} \quad (1)$$

(see Sim & Jordan 2003b for definitions of the quantities in this and the following equation). A first-cut DEMD was used to compute fluxes (F_*) for each of observed multiplets using the integral

$$F_* = \int K(T_e) \frac{\mathrm{d}Em}{\mathrm{d}\log T_e} \, \mathrm{d}\log T_e \quad . \quad (2)$$

These were compared with the observed fluxes. The DEMD was then modified iteratively until reasonable agreement ($\sim$ 50 per cent) was obtained between the fluxes predicted by the DEMD and the observed fluxes. Greatest weighting was given to the density-insensitive lines. During this process, it was assumed that the DEMD remains smooth on scales $\Delta \log T_e[\mathrm{K}] < 0.1$ dex, which is comparable to the typical scale of overlap between adjacent emission measure loci from the *STIS* data.

The DEMD was only specified over the temperature range $3.8 < \log T_e[\mathrm{K}] < 5.5$ since outside this range there are insufficient lines to provide robust constraints. This means that lines that form partially outside this temperature range (in particular those of O VI and O V) will be underpredicted by the DEMD. The resulting DEMD (DEMD-A) was used to compute a mean EMD (EMD-A) which is overplotted in Figs. 2, 3 and 5. The fluxes computed from DEMD-A using equation (2) are compared with observed fluxes in Table 7.

DEMD-A predicts fluxes for most of the high-temperature, optically thin lines (C III, C IV, N V, Si III, Si IV, S IV, N IV, O III) that are in agreement with the observations to within $\sim$ 30 per cent, which is comparable to the likely measurement errors for the weak lines, and the uncertainty in the ionisation balance for the alkali-like ions. Among the high-temperature lines, the poorest agreement is for O IV 1400 Å and S IV 1070 Å. Both of these multiplets have already been identified as anomalous from the EMD loci discussed above. Note that for both Al III and S VI the underprediction is probably the result of errors in the ionisation balance – these are both alkali-like ions for which the finite density has not been accounted for in the recombination rates (see Section 3).

Among the lower-temperature ions (C II, Mg II and Si II) the agreement is less good. However, these multiplets are likely to be affected by opacity (making equation 2 invalid) – their discussion is postponed to Section 5 where full radiative transfer calculations are presented.

5 THE PRELIMINARY ATMOSPHERIC MODEL

5.1 Construction of the model

In this and subsequent sections, EMDs are used to construct new atmospheric models for ϵ Eri. These models are used to perform ra-

Table 7. Comparison of calculated fluxes (F_c) and observed fluxes (F_o) for emission measure distribution DEMD-A. The error column gives the percentage error on the measured flux. The top part of the table gives the density-insensitive *STIS* lines, the middle part gives the density-sensitive *STIS* lines and the lower part gives the *FUSE* lines.

Ion	λ (Å)	% error	$(F_c - F_o)/F_o \times 100\%$
C II	1335	3	-7
C III	1175	10	13
C IV	1550	2	-19
N V	1240	4	-29
O V	1371	5	-40
Mg II	2800	2	-41
Al III	1854	12	-60
Si II	1810	1	-55
Si II	1530	1	-68
Si II	1308	5	-80
Si II	1260	13	-67
Si II	1195	30	-71
Si III	1206	3	-17
Si IV	1400	3	-29
S II	1255	10	-4
S IV	1406	20	9
N IV	1486	33	30
O III	1663	17	16
O IV	1400	6	89
O V	1218	6	-22
Si III	1892	4	5
Si III	1300	7	-22
C II	1010	25	30
C II	1037	6	56
C III	977	2	52
C III	1175	2	11
N III	991	24	35
O VI	1035	4	-50
Si III	1110	30	12
S IV	1070	43	125
S VI	933	33	-68

diative transfer calculations for the important optically thick lines, the results of which are then discussed.

The atmospheric models presented are all constructed in one-dimension under the assumption of hydrostatic equilibrium, including both thermal and microturbulent contributions to the pressure. Full details of the method of constructing atmospheric models from EMDs are presented elsewhere (see e.g. Griffiths & Jordan 1998 and Harper 1992 for all the relevant background or Sim 2002 for a complete discussion of the iteration scheme used here). The Thatcher et al. (1991) model is used to describe the atmosphere below the temperature range to which the DEMD extends ($\log T_e[\mathrm{K}] < 3.8$).

An important ingredient in the modelling is the microturbulent velocity in the chromosphere/transition region. Sim & Jordan (2003a) used line width measurements from the ϵ Eri ultraviolet data to determine the most-probable non-thermal speed ($\xi(T_e)$) in the upper atmosphere. For the models presented here, these results have been fitted with the simple form

$$\xi(T_e) = \left\{ \begin{array}{cc} -31.56 + 10.716 \log T_e & 3.8 < \log T_e < 4.9 \\ 20.95 & \log T_e > 4.9 \end{array} \right\} \mathrm{km\ s^{-1}} \quad (3)$$

which is an adequate representation of the line-width measurements. Initially, it is assumed that *all* the observed non-thermal motion can be classified as microturbulence (i.e. $\xi(T_e)_{\mathrm{micro}} = \xi(T_e)$). Later, a small amount of macroturbulence is introduced (Section 6). For $\log T_e[\mathrm{K}] < 3.8$, the microturbulence is extrapolated linearly in $\log T_e$ to agree with the measured photospheric microturbulent velocity (1.25 km s^{-1}; Drake & Smith 1993) at the temperature minimum.

5.2 Radiative transfer calculations

Radiative transfer calculations were performed with the MULTI code (Scharmer & Carlsson 1985a,b; Carlsson 1986). In addition to the atmospheric models, as input MULTI requires atomic models for the ions that give rise to the lines under consideration. Brief details of the adopted atomic models are given below.

5.2.1 Hydrogen

The H model used contains levels $n = 1$ to $n = 8$ and the continuum. The radiative transfer calculations for H make use of the Hubeny & Lites (1995) modifications to MULTI which allow the effects of Partial Redistribution (PRD) to be taken into account for Lyman α and β. (See Hubeny & Lites 1995 and Sim 2001 for discussions of PRD effects in cool star atmospheres.)

5.2.2 Magnesium

A ten level Mg model, developed by P. Judge, was used. The model describes the first three ionisation stages of Mg. PRD is included in the h and k-lines of Mg II using the Uitenbroek (1989) modifications to MULTI.

5.2.3 Silicon

In view of the large number of Si lines observed in the *STIS* data, a new 36 level model of Si has been constructed. This model focuses on Si II – IV and contains the ground states of Si I and Si V, for the sake of the ionisation calculations. The metastable $3p^2\ ^1D$, ^1S and $3s3p^3\ ^5S$ levels of Si I are also included. 51 radiative transitions are included in the model (all treated with Complete Redistribution [CRD] only). The atomic data for these transitions (gf-values and rates for collisional excitation by free electrons) were extracted from the CHIANTI database. Recombination rates (radiative plus dielectronic) were taken from Summers (1974a,b, see Section 2) and photoionisation rates were obtained from the on-line Opacity Package database (Cunto et al. 1993). Collisional ionisation rates and charge exchange rates for collisions with both hydrogen and helium were taken from Arnaud & Rothenflug (1985).

5.2.4 Carbon

A new 33 level model for C has been constructed to complement the new Si model. Like the Si model it is focused on the second to fourth ionisation stages, containing only the ground states of the first and fifth stages for the ionisation calculations. 52 radiative transitions are included in the model (all treated with CRD). The atomic data were drawn from the same sources as used for the Si model.

Table 8. Fluxes computed using MULTI (F_c) compared with observed fluxes (F_o) for lines of H, Mg, Si and C. F_c is given in units of 10^{-13} ergs cm^{-2} s^{-1}. The first section gives the density- insensitive lines from the *STIS* spectrum, the second gives the density-sensitive lines from *STIS* and the third gives the lines from *FUSE*. Computed fluxes are given for models A, B, C and D. Following the model B fluxes, values are given for computations from a model identical to model B except that the Asplund et al. (2004) relative abundances are adopted.

Ion	λ_0	F_c				$(F_c - F_o)/F_o \times 100\%$			
	(Å)	Model A	Model B	Model C	Model D	Model A	Model B	Model C	Model D
H I[a]	1215.671	634.	441 (410)	302	220	124	176 (156)	88.8	37.5
C II[a]	1334.532	3.30	3.41 (2.49)	1.63	3.25	75.5	81.4 (32.4)	-13.3	72.9
C II	1335.68 bl.	8.29	8.68 (6.26)	4.04	8.81	71.3	79.3 (29.3)	-16.5	82.0
C III	1174.933	0.541	0.556 (0.404)	0.453	0.589	32.0	35.6 (-1.5)	10.5	43.7
C III	1175.263	0.425	0.437 (0.318)	0.357	0.441	3.7	6.6 (-22.4)	-12.9	7.6
C III	1175.69 bl.	1.908	1.961 (1.429)	1.602	1.976	28.1	31.6 (-4.1)	7.5	32.6
C III	1175.987	0.421	0.433 (0.315)	0.353	0.438	2.7	5.6 (-23.2)	-13.9	6.8
C III	1176.370	0.528	0.543 (0.395)	0.444	0.545	14.8	18.0 (-14.1)	-3.5	18.5
C IV	1548.187	3.83	4.39 (3.19)	4.32	4.36	-31.5	-21.5 (-42.9)	-22.7	-22.0
C IV	1550.772	1.92	2.20 (1.59)	2.16	2.18	-31.9	-22.0 (-43.6)	-23.4	-22.7
Mg II[a]	2796.352	314.	348 (312)	351	213	3.0	14.1 (2.3)	15.1	-30.2
Mg II[a]	2803.531	196	218 (193)	228	138	-15.5	-6.0 (-16.8)	-1.7	-40.5
Si II	1190.416	0.031	0.060 (0.055)	0.074	0.056	-69.0	-40.0 (-45.0)	-26.0	-44.0
Si II	1193.290	0.033	0.057 (0.054)	0.075	0.043	-63.3	-36.7 (-40.0)	-16.7	-52.2
Si II	1194.500	0.092	0.131 (0.122)	0.170	0.101	-48.9	-27.2 (-32.2)	-5.6	-43.9
Si II	1197.394	0.013	0.034 (0.033)	0.045	0.028	-87.0	-66.0 (-67.0)	-55.0	-72.0
Si II[a]	1260.422	0.154	0.215 (0.192)	0.262	0.183	-19.4	12.6 (0.5)	37.2	-4.2
Si II	1264.738	0.305	0.450 (0.400)	0.530	0.404	-39.6	-10.9 (-20.8)	5.0	-20.0
Si II	1265.002	0.065	0.107 (0.094)	0.119	0.107	-62.2	-37.8 (-45.3)	-30.8	-37.8
Si II	1304.370	0.047	0.075 (0.066)	0.085	0.071	-64.7	-43.6 (-50.4)	-36.1	-46.6
Si II	1309.276	0.071	0.107 (0.095)	0.126	0.096	-68.0	-51.8 (-57.2)	-43.2	-56.8
Si II	1526.707	0.294	0.570 (0.508)	0.661	0.478	-42.1	12.2 (0.0)	30.1	-5.9
Si II	1533.431	0.405	0.764 (0.685)	0.933	0.604	-33.1	25.9 (12.9)	53.7	-0.5
Si II	1808.013	3.28	5.90 (5.23)	5.69	5.31	-48.7	-7.7 (-18.2)	-11.0	-16.9
Si II	1816.928	6.49	11.26 (10.00)	10.76	9.55	-37.7	8.1 (-4.0)	3.3	-8.3
Si II	1817.451	1.57	2.61 (2.29)	3.18	2.67	-50.9	-18.4 (-28.4)	-0.6	-16.6
Si III	1206.500	3.34	3.47 (3.09)	4.05	4.05	-7.2	-3.6 (-14.2)	12.5	12.5
Si IV	1393.755	1.53	1.561 (1.396)	3.052	1.556	-33.5	-32.1 (-39.3)	32.7	-32.3
Si IV	1402.770	0.772	0.787 (0.704)	1.538	0.783	-36.2	-35.0 (-41.8)	27.1	-35.3
Si III	1294.545	0.038	0.038 (0.034)	0.047	0.039	-26.9	-26.9 (-34.6)	-9.6	-25.0
Si III	1296.726	0.030	0.030 (0.027)	0.037	0.031	-26.8	-26.8 (-34.1)	-9.8	-24.4
Si III	1298.93 bl.	0.134	0.135 (0.121)	0.166	0.138	-19.8	-19.2 (-27.5)	-0.6	-17.4
Si III	1301.149	0.025	0.025 (0.023)	0.029	0.025	-10.7	-10.7 (-17.9)	3.6	-10.7
Si III	1303.323	0.037	0.037 (0.034)	0.046	0.038	-40.3	-40.3 (-45.2)	-25.8	-38.7
Si III	1892.030	1.25	1.19 (1.07)	1.37	1.30	0.0	-4.8 (-14.4)	9.6	4.0
H I[a]	972.537	2.81	2.80 (2.73)	2.02	1.05	329	344 (333)	221	66.7
H I[a]	1025.722	10.46	11.02 (10.69)	7.74	4.84	172	201 (192)	111	32.2
C II	1009.858	0.018	0.019 (0.013)	0.009	0.020	50.0	58.3 (8.3)	-25.0	66.7
C II	1010.083	0.037	0.037 (0.027)	0.018	0.039	37.0	37.0 (0.0)	-33.3	44.4
C II	1010.371	0.055	0.055 (0.040)	0.027	0.058	19.6	19.6 (-13.0)	-41.3	26.1
C II[a]	1036.337	0.448	0.403 (0.289)	0.192	0.420	273	236 (141)	60.0	250
C II	1037.018	0.681	0.627 (0.454)	0.304	0.611	134	116 (56.0)	4.5	110
C III	977.020	8.85	9.09 (6.45)	6.76	9.99	89.5	94.6 (38.1)	44.8	114
C III	1174.933	0.541	0.556 (0.404)	0.453	0.589	24.4	27.8 (-7.1)	4.1	35.4
C III	1175.263	0.425	0.437 (0.318)	0.357	0.441	0.0	2.8 (-25.2)	-16.0	3.8
C III	1175.69 bl.	1.908	1.961 (1.429)	1.602	1.976	25.6	29.1 (-5.9)	5.5	30.1
C III	1175.987	0.421	0.433 (0.315)	0.353	0.438	4.0	6.9 (-22.2)	-12.8	8.1
C III	1176.370	0.528	0.543 (0.395)	0.444	0.545	13.1	16.3 (-0.15)	-4.9	16.7
Si III	1108.358	0.023	0.023 (0.021)	0.030	0.023	15.0	15.0 (5.0)	50.0	15.0
Si III	1109.96 bl.	0.065	0.066 (0.059)	0.085	0.067	0.0	1.5 (-9.2)	30.8	3.1
Si III	1113.20 bl.	0.131	0.133 (0.119)	0.174	0.136	8.3	9.9 (-1.7)	43.8	12.4

[a] Line affected by interstellar absorption.

5.3 Model A

Using the assumptions mentioned in Section 5.1, DEMD-A was used to compute a new atmospheric model for the chromosphere/lower transition region. This model was used by Sim & Jordan (2003a); the most important atmospheric parameters (T_e, P_e, P_H) are shown in their fig. 3.

Together with the atomic models discussed in Section 5.2, Model A was used to compute fluxes for the observed lines of H I, C II – IV, Mg II and Si II – IV. These fluxes are given in Table 8, where they are compared with the observed fluxes. For comparison, the run of electron temperature against mass column density from the Thatcher et al. (1991) model was also used to compute fluxes – these are given in Table 9. Since the Thatcher et al. (1991) model was developed using chromospheric lines, only lines of relatively low temperature ions are listed in Table 9 – for all of the higher-temperature lines (which were outside the scope of their study) the Thatcher et al. (1991) model substantially overpredicts the fluxes.

In general, model A can reproduce the observed fluxes of Mg II, C III – IV and Si III – IV within an accuracy of several tens per cent (see Table 8). The poorest agreement for lines of these ions is for C III 977 Å, the observed flux for which may be subject to significant uncertainty due to the correction for channel drift in the *FUSE* spectrum.

The greatest failings of model A relate to C II and Si II; although the weak C II 1010-Å multiplet is predicted to within observational errors (almost), the strong resonance multiplets (1335 Å and 1037 Å) are overpredicted by factors of ~ 2. These multiplets are predicted to be significantly stronger by the radiative transfer calculations (Table 8) than the optically thin approximation (Table 7) – this is due to scattering in the lines (see Section 5.3.3). Although interstellar absorption affects C II 1334.5 Å and 1036.3 Å, it cannot be responsible for the discrepancies in the stronger 1335.7-Å and 1037.0-Å lines. In contrast, the strong Si II lines are *all* underpredicted by as much as 70 per cent. Although the Thatcher et al. (1991) model does slightly better than model A for some of the chromospheric Si II lines, it does much less well for the hotter transition region lines (i.e. C II) – as noted above, the Thatcher et al. (1991) model was not developed to address the transition region in detail.

While small alterations to the DEMD could improve the agreement amongst the higher temperature lines, it is not possible to simply attribute these results to failings in the determination of the DEMD. By examining the emission measure loci in Figs. 2 and 5, it is clear that the C II lines form over a wide range $4.0 < \log T_e(\mathrm{K}) < 4.5$. To reduce the predicted C II resonance line fluxes would require the DEMD to be reduced in this temperature range. However, this cannot be done without reducing the predicted fluxes of Si III or Si II which form in the same temperature range. Such a reduction is unacceptable since the Si III fluxes are not overpredicted by model A, and the Si II fluxes are already underpredicted to a significant extent. That simple modifications to the DEMD cannot account for the C II/Si II discrepancy was checked by constructing ~ 20 different models with modified DEMDs, none of which were able to significantly improve the predicted C II fluxes without substantial adverse effects on the Si II and/or III fluxes.

Therefore, an alternative explanation is required for the C II/Si II discrepancy. Potential explanations are discussed below and used in Section 5.4 to construct two more models for the outer atmosphere of ϵ Eri (models B and C).

Table 9. Fluxes computed using MULTI (F_c) and the Thatcher et al. (1991) model compared with observed fluxes (F_o) for lines of H, Mg, Si II and C II. F_c is given in units of 10^{-13} ergs cm^{-2} s^{-1}. The upper section gives the lines from the *STIS* spectrum and the lower gives the those from the *FUSE* spectrum.

Ion	λ_0 (Å)	F_c	$(F_c - F_o)/F_o \times 100\%$
H I[a]	1215.671	1175	639
C II[a]	1334.532	67.9	3512
C II	1335.68 bl.	213.9	4319
Mg II[a]	2796.352	398	30.5
Mg II[a]	2803.531	256	10.3
Si II	1190.416	0.377	277
Si II	1193.290	0.381	323
Si II	1194.500	0.829	361
Si II	1197.394	0.256	156
Si II[a]	1260.422	1.02	434
Si II	1264.738	2.03	302
Si II	1265.002	0.470	173
Si II	1304.370	0.303	128
Si II	1309.276	0.455	105
Si II	1526.707	1.07	111
Si II	1533.431	1.53	152
Si II	1808.013	6.26	-2.0
Si II	1816.928	11.75	12.8
Si II	1817.451	2.89	-9.7
H I[a]	972.537	9.70	1440
H I[a]	1025.722	29.0	692
C II	1009.858	1.32	10900
C II	1010.083	2.25	8233
C II	1010.371	2.98	6378
C II[a]	1036.337	19.4	16067
C II	1037.018	22.1	7495

[a] Line affected by interstellar absorption.

5.3.1 *Atomic data for Si* II

The limitations of the atomic data used in the radiative transfer calculations are almost certainly partially responsible for the apparent discrepancy amongst lines of Si II.

The most important uncertainties are in the electron collision rates. The rates used in the Si II model are from Dufton & Kingston (1991). Although it is difficult to asses the accuracy of collision rates, Dufton & Kingston (1991) suggest that their rates should be accurate to at least ± 20 per cent. Their calculations give rates between the ground ^{2}P levels and all the excited states used in the Si II model, and between the metastable ^{4}P and excited 3s3p^2 ^{2}D levels (which give rise to the 1810-Å multiplet), but no collision rates are provided from the ^{4}P levels to other excited states. The absence of excitation rates from the metastable ^{4}P states may mean that the populations of all the excited states above 3s3p^2 ^{2}D are underestimated – this would cause the 1530, 1260, 1309 and 1190-Å multiplets to be systematically underpredicted. Assuming that the collision strengths from the ^{4}P states to levels higher than 3s3p^2 ^{2}D are the same as those to the 3s3p^2 ^{2}D$_{3/2}$ level, it is found that the predicted fluxes in the multiplets mentioned above are increased by 53, 25, 73 and 32 per cent, respectively. Although only a crude estimate, this suggests that excitation from ^{4}P could be important and may explain why many of the Si II transitions are significantly underestimated by the models.

In addition to direct excitation from the ground state, the 4s ^{2}S

level population is significantly affected by collisional excitation to 4p ^{2}P followed by radiative decay (Jordan 1969b). Thus the computed 1530-Å flux is probably subject to the largest uncertainties due to the atomic data. The 1810-Å flux is subject to the smallest uncertainties, being dominated by the errors in the collision rates between the low-lying levels (at most a few tens per cent). (See also Jordan et al. 2001a.)

5.3.2 Atomic data for C II

The collision rates for C II are from Blum & Pradhan (1992) who give rates between all levels that are relevant to the formation of the 1335 and 1037-Å multiplets. The authors suggested that these rates are accurate to between 20 per cent and a factor of 2, with greater uncertainty for higher levels. This suggests that the data should be better for the 1335-Å multiplet than for the 1037-Å multiplet.

5.3.3 Geometric complications

The C II resonance line fluxes are computed to be significantly larger when radiative transfer is taken into account, compared to the optically thin limit (compare Tables 7 and 8). This is because the calculations in Section 4.5 and Table 7 assume that the fraction of photons emitted in a particular line which escape the atmosphere is $\simeq 1/2$, as given by the usual geometric dilution factor (the optically thin limit). For scattering dominated optically thick lines (such as the C II resonance lines) that assumption *underestimates* the surface flux since scattering turns around many of the photons that are initially emitted downwards into the atmosphere so that they eventually emerge through the upper boundary. For a plane-parallel layer this backscattering effect can increase the flux by up to a factor of two (for a comprehensive discussion of this and related effects in the solar case, see Pietarila & Judge 2004). In the MULTI calculations presented here, the intensity is computed at the surface of the star as a function of both wavelength and angle accounting for radiative transfer effects (including backscattering) and this is integrated over angles to compute the flux. Thus for an homogeneous, plane-parallel atmosphere, the results presented in Section 5.2 and Table 8 are more reliable than those given in Section 4.5.

In a real stellar atmosphere, however, the situation is more complex; assuming that ϵ Eri is like the Sun, the transition region emission will mostly originate in the bright supergranulation cell boundaries which occupy only a fraction of the stellar surface (see, for example the solar C II lines discussed and modelled by Judge, Carlsson & Stein 2003). We have derived a filling factor of emitting material in the upper transition region of ϵ Eri of ~ 0.2 (Sim & Jordan 2003b). In such a geometry, much of the emission will not travel solely within the cell boundary material but will escape sideways into the cell interiors which are likely to be hotter and less dense. This will alter the probability that the emission is subsequently scattered upward to escape from the star. Thus a single-component model may be expected to predict erroneously large fluxes for lines in which there is significant scattering opacity. (See also Jordan, Smith & Houdebine 2005.)

The simplest test for this interpretation of the overprediction of the C II resonance line fluxes is to examine C II lines that are not affected by back-scattering. Unfortunately the ideal lines for this examination (the optically thin C II $2s^2 2p\ ^2P - 2s2p^2\ ^4P$ lines) are too weak to measure in the STIS spectrum and all the model predictions are consistent with this non-detection. The only lines that can be used for this test are the weak C II 1010-Å lines in the *FUSE* spectrum; the strongest of these lines is measured to an accuracy of 15 per cent. Since they originate in a relatively high-lying energy level, the atomic data (collision rates) for these lines are likely to be significantly poorer than for the other C II lines discussed here. Nevertheless, these lines are *not* significantly overpredicted by model A (the strongest line agrees with the observations to within 20 per cent). Since the lines of the 1010-Å multiplet are not affected by back-scattering this supports the argument that the discrepancy between the observed and computed C II resonance line fluxes originates in the treatment of scattering in such lines.

In order to test the hypothesis that the overprediction of the C II resonance lines is due to the simplistic 1-D geometry, multi-component models need to be constructed and used to perform multi-dimensional radiative transfer calculations. Such work lies beyond the scope of this paper. In Section 6 a complete atmospheric model (model B) is constructed under the hypothesis that the C II/Si II discrepancy is due to errors in the computed C II resonance line fluxes. This model has been used to perform a test (based on the observed Cl I line) which probes the C II resonance line strength *within* the atmosphere. That test supports the evidence from the 1010-Å multiplet that the discrepancy lies in the computation of the C II resonance line surface fluxes.

5.3.4 Abundances

An alternative explanation for the C II/Si II discrepancy is an error in the assumed abundances. As mentioned in Section 4.1, the relative abundances adopted here are based on the solar values given by Grevesse & Sauval (1998). Recently, Asplund et al. (2004) presented a new set of solar abundances which differ in the logarithm from those of Grevesse & Sauval (1998) by -0.13, -0.14, -0.17 and -0.04, for C/H, N/H, O/H and Si/H, respectively. Given that the relative changes of C, N and O are very similar (factors of 1.35 to 1.48) they will have little influence on the shape of the EMD deduced based on lines of these elements – if these new abundances were adopted, a small global increase in the EMD (equivalent to a small reduction in the adopted metallicity of ϵ Eri) would lead to computed fluxes which differ only very slightly from those obtained using the earlier abundances. Adopting the new abundances, however, would alter the relative abundance of C to Si by a factor of 1.23. Although this factor would act in the correct sense to address the C II/Si II problem here, it is insufficient to explain most of the discrepancy. Therefore, the standard Grevesse & Sauval (1998) abundances will be retained throughout this investigation (although the influence of adopting the Asplund et al. 2004 abundances will be quantified in Section 6.3).

To bring the C II resonance lines and Si lines into agreement, either the C abundance could be made smaller or the Si abundance made larger. If the assumed abundances were wrong, one would expect to see a discrepancy between the lines of higher ions (C III, IV or Si IV) and lines of other species. Unfortunately, neither C IV nor Si IV are ideal for comparison since they are very sensitive to the ionisation balance calculation (Section 3). The observed O III lines form at similar temperatures to the C III 1175-Å multiplet and the Si IV lines. Based on the multiplet fluxes in Table 7, there is no obvious discrepancy between O III and C III. Si IV is different, however, being underpredicted rather than overpredicted; thus it is concluded that if abundance variations are responsible for the C II/Si II it is the Si abundance that is likely to be in error.

In order to remove the C II/Si II discrepancy, the Si abundance needs to be increased by about a factor of 2.4, relative to

the value adopted in model A. The interpretation of such an increase requires some care. Abia et al. (1988) have measured the photospheric Si abundance in ϵ Eri. They found the logarithmic Si abundance relative to the Sun to be $[\mathrm{Si/H}] = -0.11$ dex. Based on their discussion of likely errors, the uncertainty in this value should not be more than ± 0.25 dex. More recent studies have found similar results: $[\mathrm{Si/H}] = -0.10$ and -0.04 (Bodaghee et al. 2003; Zhao et al. 2002, respectively) with much smaller errors (~ 0.05 dex). These measurements are all consistent with the assumed metal abundances in model A which are based on Drake & Smith (1993). It suggests, therefore, that a proposed increase in the transition region Si abundance would be an increase *relative to the stellar photospheric abundance*. Note that Zhao et al. (2002) deduce a C abundance which is *slightly higher* than solar and thus, if adopted, would make the discrepancy worse. However, since their C analysis involves only one spectral line the error in this result may be significantly larger than that in the Si abundance.

It is concluded that if abundance variations are responsible for the C II/Si II discrepancy, the Si abundance enhancement required is relative to the ϵ Eri photospheric abundance. There is considerable interest in the relative abundance of elements in the transition regions and coronae of cool stars. Many authors (see for example Jordan et al. 1998 and references therein), have discussed the possibility that the relative abundances of elements in the corona are different from those in the photosphere to a degree which correlates with the *First Ionisation Potential* (FIP) of the element. It is suggested that, in the upper atmosphere, elements with high FIPs (> 10 eV) have lower abundances relative to those with low FIPs. The first evidence of this "FIP-effect" was found in the solar wind (Crawford, Price & Sullivan 1972). The physical origin of the effect is unknown. Based on studies of the solar atmosphere, Feldman et al. (1992) give coronal elemental abundances, assuming that the FIP-effect acts to increase the low-FIP element abundances. They give a relative coronal abundance for Si to C which is a factor 3.8 greater than the photospheric relative abundance. Laming, Drake & Widing (1995) used full disk solar observations to confirm the coronal abundances given by Feldman et al. (1992). Their work found evidence of the FIP-effect in the corona, but they found no suggestion of a FIP-effect operating at lower temperatures ($\log T_e(\mathrm{K}) < 6$). Jordan, Macpherson & Smith (2001) studied spatial variations in the Si III/C II intensity ratio across regions of the quiet Sun and a coronal hole. They found no differences in excess of 0.2 dex. Since the FIP effect is not thought to operate in coronal holes this suggests that the FIP enhancement of Si in the quiet Sun is less than a factor of 1.6. These results are surprising. Since the first ionisation for most elements takes place at chromospheric temperatures, one would expect an effect associated with the first ionisation potential to originate in the chromosphere and thus to be apparent in the transition region, but the solar work suggests that the effect only occurs at significantly higher temperatures.

Several studies have examined the case for a FIP-effect in other cool stars. Laming, Drake & Widing (1996) looked for a FIP-effect in the corona of ϵ Eri. They found some evidence for a solar-like FIP-effect, but were unable to make a definitive detection. More recently, Drake, Laming & Widing (1997) and Laming & Drake (1999) have identified solar-like FIP-effects in the coronae of α Cen and ξ Boo. It has also been found, however, that there is no apparent FIP-effect in the corona of Procyon (Drake, Laming & Widing 1995).

In summary, to date, there is no compelling evidence for the operation of a FIP-effect in the chromospheres/transition regions of the Sun or any other late-type stars. If there is such an effect in the coronae of stars, however, it is difficult to understand why it would not occur in the lower parts of the atmosphere. The C II/Si II discrepancy in the modelling of ϵ Eri could be interpreted as evidence for a FIP enhancement of the Si abundance in the low atmosphere of up to a factor of 2.4, and an atmospheric model based on that assumption is constructed in Section 6 (model C). There are, however, significant uncertainties and several shortcomings for this explanation which are also discussed in Section 6.

6 MODELS B AND C

In this section, the discussion of model A (Section 5.3) is used to develop two more models (B and C). These models were constructed in the same manner as model A (see Section 5.1) but are based on different EMDs for the transition region and include a small amount of macroturbulence. The differences between models B and C relate to the possible interpretations of the C II/Si II discrepancy identified in model A (see below). The complete atmospheric models (A, B and C) are tabulated in Appendix B.

6.1 Modifications to the turbulent velocity field

For model A it was assumed that all the observed non-thermal motion was due to microturbulence. Since the optically thick chromospheric line profiles are sensitive to the distinction between macroturbulence and microturbulence, the radiative transfer calculations for model A can be used to improve the prescription for the turbulence in the new models B and C.

In Fig. 6, the computed Mg II h and k lines are plotted with the observed line profiles from STIS. Clearly the central reversal in the model A profiles is too wide, indicating that the assumed microturbulence is too large. To compensate for this, macroturbulence is invoked to explain some of the observed line width: by trial and error, it was found that a value of $\xi_{\mathrm{macro}} = 8.5$ km s^{-1} leads to much better profiles for the Mg II lines. Unfortunately, there are no suitable lines to derive the macroturbulence in other parts of the atmosphere and so it is simply assumed that the macroturbulence does not vary through the upper chromosphere and transition region: thus for models B and C, the microturbulent velocity field used above $\log T_e[K] = 3.8$ is

$$\xi^2_{\mathrm{micro}}(T_e) = \xi^2(T_e) - \xi^2_{\mathrm{macro}} \tag{4}$$

where $\xi(T_e)$ is the non-thermal velocity specified by equation (3). The adopted value for the macroturbulence has little significance above the low transition region, where it leads to less than 10 per cent difference in the adopted microturbulence.

6.2 Modifications to the EMD

For both models B and C the EMD has been slightly modified at high temperatures to improve the agreement between some of the predicted and observed line fluxes. In addition, more significant modifications have been made at low temperatures; these modifications are discussed further below. The complete EMDs for the models are compared with that for model A in Fig. 7, and the atmospheric models obtained from the EMDs are compared with model A and the earlier models by Thatcher et al. (1991) and Kelch (1978) in Fig. 8.

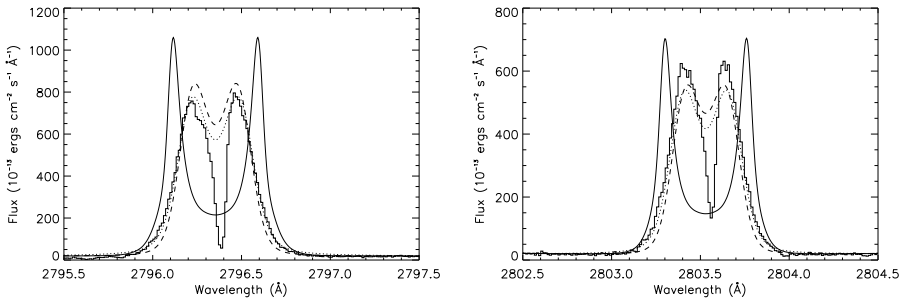

Figure 6. Comparison of computed and observed Mg II profiles. In each figure the solid histogram shows the data, the solid curve shows the model A calculations, the dashed curve shows the model B calculations and the dotted curve shows the model C calculations. The narrow dips in the observed profiles are due to interstellar absorption.

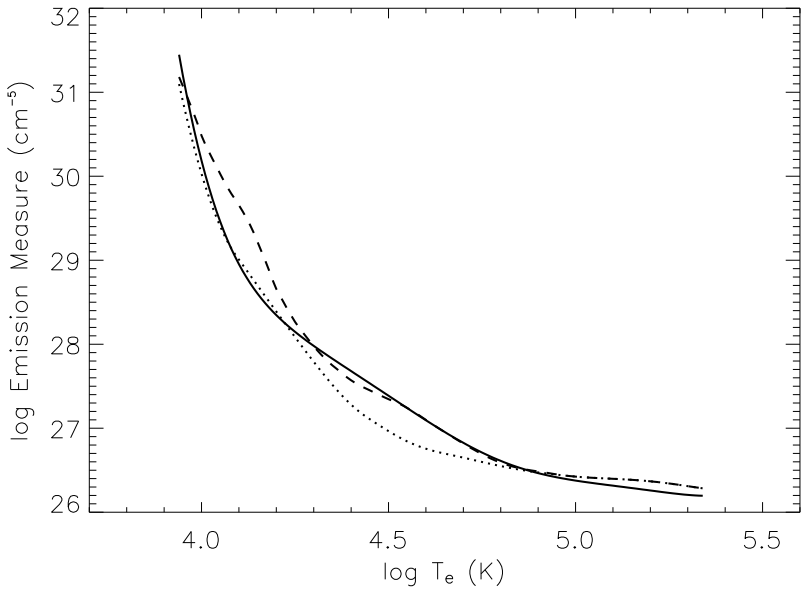

Figure 7. Comparison of mean emission measure distributions. The solid curve is for model A, the dashed curve is for model B and the dotted curve is for model C. In each case the mean emission measure $Em^{0.3}(T_e)$ is plotted.

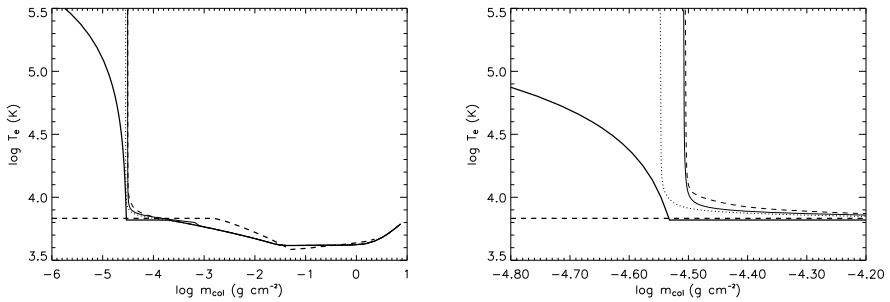

Figure 8. Comparison of atmospheric models (column mass density versus electron temperature). The left panel shows the complete models and the right panel shows the transition region in detail. The heavy dashed line is the Kelch (1978) model, the heavy solid line is the Thatcher et al. (1991) model, the light solid line is model A, the light dashed line is model B and the dotted line is model C.

6.2.1 Model B

Model B has been constructed based on the assumption that the discrepancy between the computed and observed C and Si fluxes is the result of errors in the computed C II resonance line surface fluxes, primarily due to the simplistic one-dimensional geometry used here (see Section 5.3.3). For this model, the DEMD was significantly increased around $\log T_e[K] = 4.0$ and slightly reduced at higher temperatures. These alterations increase the computed Si II fluxes and slightly reduce the C II and Si III fluxes relative to model A.

6.2.2 Model C

Model C has been developed to investigate the alternative explanation of the C II/Si II discrepancy in model A, that of a (possibly FIP-related) change in the Si abundance. For this model, the assumed Si abundance was increased by a factor of 2.4. If this increase is due to a FIP-related effect then one would expect that the abundances of other low-FIP elements should be increased by a similar factor. Of the other element considered here this affects Mg and Al – hence the Mg and Al abundances have also been raised by a factor of 2.4 relative to those in model A.

The DEMD for model C was reduced throughout the region $\log T_e[K] < 4.5$ (compared with DEMD-A) to allow for the change in the emission measure loci resulting from the higher low-FIP-element abundances.

Table 10. Comparison of calculated fluxes (F_c) and observed fluxes (F_o) for emission measure distribution models B and C. Following the model B fluxes, values are given for computations from a model identical to model B saving that the Asplund et al. (2004) relative abundances are adopted. F_c given in units of 10^{-13} ergs cm^{-2} s^{-1}. The top part of the table gives the density-insensitive lines, the middle gives the density-sensitive line and the lower part gives the *FUSE* lines.

Ion	λ (Å)	F_c		$(F_c - F_o)/F_o \times 100\%$	
		Model B	Model C	Model B	Model C
N V	1240	1.27 (0.92)	1.27	-10 (-34)	-10
O V[a]	1371	0.078 (0.053)	0.078	-25 (-50)	-25
Al III	1854	0.204 (0.162)	0.218	-60 (-68)	-57
S II	1255	0.190 (0.123)	0.100	-2 (-37)	-48
S IV	1406	0.090 (0.058)	0.088	21 (-21)	19
N IV	1486	0.069 (0.050)	0.068	52 (11)	52
O III	1663	0.213 (0.144)	0.196	19 (-17)	9
O IV	1400	0.815 (0.551)	0.814	129 (55)	129
O V[a]	1218	0.671 (0.454)	0.671	-1 (-33)	-1
N III	991	0.452 (0.327)	0.409	37 (-1.0)	24
O VI[a]	1035	3.94 (2.66)	3.94	-43 (-61)	-43
S IV	1070	0.240 (0.155)	0.238	156 (65)	153
S VI	933	0.100 (0.065)	0.100	-58 (-73)	-58

[a] Flux likely to be underestimated since the line forms partially outside the temperature range covered by the models.

6.3 H Lyman line profiles

Since the cores of the strong H I Lyman lines are heavily affected by interstellar absorption, the diagnostic power of these lines for studying the stellar atmosphere lies in examining the line wings. Fig. 9 compares the Lyman α, β and γ line profiles computed from models B and C with the observations. The model profiles have been corrected for interstellar absorption using the H I column densities and velocities derived for the ϵ Eri line-of-sight by Dring et al. (1997).

For Lyman β and γ, models B and C both predict the profiles very well. Model B tends to slightly overpredict the line strength but only by 10 – 20 per cent. For Lyman α the agreement is less good – both models predict profiles with significantly weaker line wings than observed. This suggests that the models underestimate the importance of photon scattering from the line core to the wings. Since this effect is not evident in the Lyman β or γ profiles (nor the Mg II profiles) it seems unlikely that this is solely the result of errors in the atmospheric velocity field – most likely it indicates the coherence fraction used in the PRD treatment of this line is too high. A detailed investigation of the Lyman α profile goes beyond the scope of this work, but to illustrate the influence of a smaller coherence fraction, Fig. 9 also shows the Lyman α profile computed from model B adopting a frequency-independent, depth-independent coherence fraction of $\gamma = 0.9$ (this is in contrast to the other calculations which use the physical γ implemented in the Hubeny & Lites 1995 code). As expected, the constant-γ calculation predicts stronger line wings bringing it into much better agreement with the data. However, there are still some significant differences in the line shape which suggest that more redistribution in needed in the line core but less to the far wings. The illustrative γ adopted is rather low compared to theoretical calculations and lower than the preferred Lyman α maximum coherence-fraction suggested by Vernazza et al. (1981) for their solar models ($\gamma = 0.98$). However, when comparing with the Vernazza et al. (1981) value, it is noted that γ is expected to be lower in ϵ Eri than the Sun since the density is higher.

6.4 Computed fluxes

The new models (B and C) have been used to compute fluxes for all the lines considered for model A. Table 8 gives the fluxes computed from radiative transfer calculations and Table 10 gives the fluxes for the high temperature multiplets for which radiative transfer calculations have not been performed (the model fluxes for these lines are obtained directly from the DEMD on the assumption that the multiplets are effectively optically thin). In both tables, the model B fluxes are followed (in parenthesis) by fluxes computed from a model identical to model B saving that it adopts the Asplund et al. (2004) relative abundances rather than those of Grevesse & Sauval (1998).

The observed Cl I 1351-Å line provides a useful probe of the C II 1335-Å radiation field *within* the atmosphere since the Cl I line forms by fluorescence, pumped by the 1335-Å transition (Shine 1983). A very simple three level Cl I model has been used to compute the 1351-Å flux. The model contains only the ground configuration ^{2}P$^{\rm o}$ states and the excited 3p^4(^{3}P)4s ^{2}P$_{1/2}$ level. The only physical processes included in the model are the two radiative transitions ^{2}P$^{\rm o}_{3/2}$ – ^{2}P$_{1/2}$ (the transition pumped by C II) and the observed transition (^{2}P$^{\rm o}_{1/2}$ – ^{2}P$_{1/2}$). The oscillator strengths were taken from Kurucz & Bell (1995). For the calculation the C II radiation field was taken from MULTI calculations with the full C model (Section 5.2.4). Table 11 gives the computed Cl I flux for both models B and C. It is to be expected that the Cl I flux may be overestimated since no levels of ionised Cl I are included in the calculation (i.e. it is assumed that the Cl I ion fraction is 1.0).

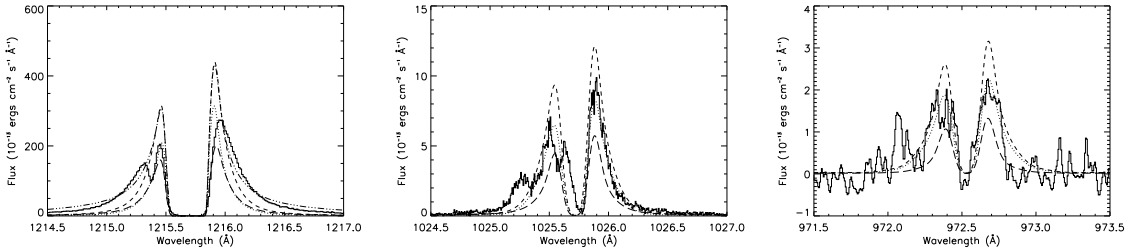

Figure 9. Comparison of computed and observed H I profiles. In each figure the solid histogram shows the data, the dashed curve shows the model B calculations, the dotted curve shows the model C calculations and the long-dashed curve shows the model D calculations. In the left panel (Ly α), the triple-dot-dash curve shows the model B result if a frequency-independent, depth-independent coherence fraction of 0.9 is adopted (see text).

Table 11. Comparison of calculated fluxes (F_c) and observed fluxes (F_o) for Cl I in models B and C. F_c given in units of 10^{-13} ergs cm^{-2} s^{-1}.

Ion	λ (Å)	F_c		$(F_c - F_o)/F_o \times 100\%$	
		Model B	Model C	Model B	Model C
Cl I	1351.656	0.231	0.110	16.7	-80.0

6.5 Discussion

The computed fluxes given in Tables 8, 10 and 11 are now used to assess the successes, failures and relative merits of models B and C. The following points are of particular note:

(i) In general, both models B and C predict fluxes for the high temperature lines (Si III and hotter) that agree well with the observations, given the combined uncertainties in the measured fluxes and atomic data (in particular the ionisation balance).

(ii) The Mg II lines are predicted well by both models, both in terms of line profile and flux. The flux ratio is slightly different from that observed, possibly indicating that there is insufficient opacity in the models. It should be noted that if inhomogeneity affects the C II lines (as postulated for model B), the Mg II lines may also be affected – but without multi-dimensional calculations the scale and nature of such an effect is unknown.

(iii) The Si II 1810-Å multiplet is well predicted (within 20 per cent) by both models. This is the most important of the Si II multiplets since it is the least sensitive to the absence of collision rates between the ^{4}P and more highly excited energy levels.

(iv) The higher excitation Si II multiplets are predicted much less accurately. However, as discussed in Section 5.3.1 these may be significantly affected by inadequacies in the Si II atomic data which may account for differences of 50 per cent or more.

(v) The C II resonance line fluxes (1335 Å and 1037 Å) are significantly overestimated by model B ($\sim$ a factor of two) but predicted quite well by model C. As discussed in Section 5.3.3 the overprediction may be the result of the simplistic geometry assumed in the models.

(vi) Although the uncertainties are large, the C II 1010-Å multiplet fluxes are *not* significantly overpredicted by model B. They are slightly underpredicted by model C.

(vii) The Cl I fluorescent flux is significantly *underpredicted* for model C. Model B predicts this line flux well.

(viii) The S II flux is more accurately predicted by model B than C.

(ix) If the Asplund et al. (2004) relative abundances are adopted, the model C II resonance line fluxes are closer to those observed but are still overpredicted. Adopting the new abundances does not significantly improve the agreement amongst the high-temperature lines since the relative abundances of C to N and O have not changed very much from those given by Grevesse & Sauval (1998).

As discussed previously, most of the exceptions to (i) can be explained by inadequacies in either the ionisation balance for alkali-like ions (Al III, S VI) or the atomic data. However, the tendency of the density-sensitive lines to be overpredicted may also indicate the presence of density inhomogeneities and, therefore, the need for multi-component modelling (see Section 4.3).

Points (vi), (vii) and (viii) all argue in favour of model B over model C. The only significant advantage of model C over model B is that it predicts the C II resonance line surface fluxes more accurately. However, model C has one more free parameter than model B (the FIP-enhancement factor) and so it is not surprising that better agreement can be found. Point (vii) is particularly crippling for model C since it suggests that the model does not reproduce the C II radiation field *within* the atmosphere.

Thus it is concluded that model B is the better single-component model for the upper transition region of ϵ Eri, and that its main limitation is the assumption of homogeneity. In future work inhomogeneous models and multi-dimensional radiative transfer must be employed to resolve the issues relating to scattering in the C II resonance lines.

The interpretation of the apparent discrepancy in the C II/Si flux ratios in terms of a variation in the abundance ratio (model C) is judged to be inferior. Model C is, however, a useful constraint on FIP-related abundance enhancement in the transition region of ϵ Eri: any enhancement in the Si abundance is constrained to be no larger than that adopted in model C (a factor of 2.4).

7 A SIMPLE MULTI-COMPONENT ATMOSPHERIC MODEL

It is well known from direct observations of the Sun and studies of other stars (e.g. the K giant α Tau, McMurry & Jordan 2000) that the atmospheres of cool stars are inhomogeneous. As mentioned in Section 5.3.3, Sim & Jordan (2003b) concluded that emitting material occupied only a limited fraction ($\sim$ 20 per cent in the mid-transition region) of the available volume in the atmosphere of ϵ Eri. All the models discussed above (A, B and C) are single-component and assume a filling factor of 100 per cent. One important consequence of a small filling factor is that line-of-sight opacities will be higher since the plasma is confined by a smaller cross-sectional area. To fully investigate multi-component atmospheric models requires multi-dimensional radiative transfer which goes beyond the scope of this paper, however, in this section a crude

two-component model will be presented and contrasted with the homogeneous models discussed above.

For the two-component model (model D) it is assumed that the atmosphere has a uniform filling factor of emitting material, fixed at 20 per cent (i.e. $A(r)/A_*(r) = 0.2$). The apparent EMD of the emitting material is the same as that used for model B. For model D the intrinsic EMD is therefore larger by a factor of 5 and hence leads to larger line opacities. The remainder of the volume is assumed to be filled by a completely dark second component. One-dimensional radiative transfer calculations are performed for the emitting component of the model neglecting the dark component. This model can only be regarded as exploratory since it neglects the probable process of photon leakage from the emitting component to the dark component but it is useful to investigate the effects of higher line opacities.

Fluxes computed from radiative transfer calculations with model D are given in Table 8. Since the EMD for model D is identical to that of model B, the model D fluxes for lines assumed to be optically thin (Table 10) are the same as those for model B. The Cl I flux for model D is also virtually identical to that of model B (Table 11).

Comparing the model B and D fluxes in Table 8 reveals several interesting changes, mostly in resonance lines that form at relatively low temperatures (these being the lines for which opacity effects are most important). The most dramatic differences are in the absolute fluxes of the strongest lines, those of H I and Mg II. Increased opacity reduces the fraction of emitted photons which eventually escape the atmosphere in these lines. The effect is greatest in the H Lyman lines where the model D fluxes are reduced by a factor ~ 2, relative to those from model B (see Fig. 9). Although this shows that the 1-D models presented here (B and C) predict the Lyman lines more accurately than the two-component model (D), it must be noted that the very simple implementation of model D neglects photon escape from the emitting component to the second component. Therefore it is expected that model D will underpredict optically thick line fluxes relative to a more sophisticated, multi-dimensional radiative transfer calculation for a multi-component atmosphere.

The Mg II lines are less affected than those of hydrogen but still decrease significantly in strength (by a factor of ~ 1.6). The computed ratio of the two Mg II lines changes in the sense which brings it closer to the observed ratio, but the change is very small.

For lines of all other ions, the changes in absolute flux are quite small, at most $\sim 10 - 20$ per cent. For some pairs of Si II lines with common upper levels (i.e. the 1526.7/1533.4-Å pair and, in particular, the 1808.0/1817.5-Å pair) the line ratios from model D are in better agreement with the data that those from model B. The provides some evidence that the line-of-sight opacities suggested by the two-component model are more realistic than those in the homogeneous models. However, the 1309.3/1304.4-Å flux ratio from model D agrees less well than that from model B (note, however, that the absolute fluxes for these lines are generally in poorer agreement with the data than those of the other lines considered here).

The C II 1334.7/1334.5-Å flux ratio changes from 2.55 in model B to 2.71 in model D, both these values being consistent with the observations, while the 1036.3/1037.0-Å ratio is in substantial disagreement with the data for both models.

It is concluded that the simple two-component model presented here is not significantly superior to the homogeneous models discussed above, although there are some improvements for the modelling of the most important Si II line ratios. A more complete treatment incorporating multi-dimensional radiative transfer effects is needed to fully investigate a multi-component model; this is deferred to later work.

8 SUMMARY AND CONCLUSIONS

Using measured ultraviolet emission line fluxes and widths, new single-component models for the upper chromosphere/transition region of ϵ Eri have been constructed; a preliminary model (model A) and two further models (models B and C) which address some of the inadequacies of the first model. To date, these models are the most detailed that have been constructed for the chromosphere/transition region of a late-type main-sequence star, other than the Sun. A simple two-component model (model D) has also been presented. The predictions of that model were only subtly different from those of the equivalent single-component model, suggesting that the 1-D modelling does provide useful average models.

For the emission measure analysis involved in the construction of the models new ionisation balance calculations have been performed which attempt to account for the density sensitivity of dielectronic recombination rates. Although not definitive, these calculations highlight the extreme sensitivity of the analysis of certain ions (generally the alkali-like ions) to errors in the recombination rates and illustrate the need for the publication of reliable recombination rates at finite density.

In most respects, line fluxes/profiles computed with the favoured model (model B) are in agreement with the observations, allowing for modest measurement uncertainties and reasonable errors in the adopted atomic data and ionisation/recombination rates. The most significant failures of the model are its inability to compute reliable fluxes for the optically thick resonance lines of C II and the spin-forbidden transition region lines of several ions (most notably O IV). Barring large errors in the atomic data, the most probable explanation for the discrepant transition region forbidden line fluxes lies with density variations in the atmosphere. The C II resonance lines have been examined in detail and used to place a constraint on possible FIP-related abundance variations within the upper atmosphere. However, it has been concluded that the anomaly associated with these lines is most likely to be related to scattering in an inhomogeneous atmosphere.

Thus the models presented here represent the limit to what can be achieved with single-component models of the outer atmospheres of late-type stars, and the single-dimensional radiative transfer calculations associated therewith; such models can account for most of the observed properties of ultraviolet emission lines, but modern spectra are of sufficient quality to indicate some inadequacies. Evidence of inhomogeneity comes as no surprise; direct observation of the Sun shows us that stellar atmospheres contain structure. However, at present we have no direct means of observing inhomogeneity in other main-sequence stars and so it can only be understood by modelling spectra.

Theoretical studies involving two-component models are already underway (e.g. Cuntz et al. 1999). In the future constraints on modelling of this type must be provided by semi-empirical multi-component modelling of spectra involving multi-dimensional radiative transfer calculations (codes capable of such multi-dimensional calculations are now available e.g. Uitenbroek 2001).

The indications of inhomogeneity in the upper chromosphere/lower transition region of ϵ Eri dovetail with our analysis of the upper transition region/corona of the same star (Sim & Jor-

dan 2003b), in which the filling factor of emitting material in the mid-transition region was found to be $\sim$ 20 per cent. Given the current absence of a definitive understanding of the heating mechanisms which operate in the lower transition region and below, a similar argument cannot be applied to directly estimate the filling factor in these parts of the atmosphere, but if the filling factor is associated with magnetic fields (as expected) then solar observations would suggest that the filling factor should become smaller deeper in the atmosphere. However, a full investigation of this must await quantitative 3-D modelling of the optically thick lines which can provide information about the inhomogeneity; it is to be hoped that in the near future such modelling can be combined with advances in theoretical studies to lead us to a clearer understanding of the structure and heating of the outer atmospheres of late-type stars.

ACKNOWLEDGEMENTS

The majority of this work was carried out while SAS was a PPARC supported graduate student at the University of Oxford (PPA/S/S/1999/02862). It was completed while he was a PPARC supported PDRA at Imperial College London (PPA/G/S/2000/00032).

Some of the data presented in this paper were obtained from the Multimission Archive at the Space Telescope Science Institute (MAST). STScI is operated by the Association of Universities for Research in Astronomy, Inc., under NASA contract NAS5-26555. Support for MAST for non-HST data is provided by the NASA Office of Space Science via grant NAG5-7584 and by other grants and contracts.

BIBLIOGRAPHY

Abia C., Rebolo R., Beckman J. E., Crivellari L., 1988, A&A, 206, 100
Arnaud M., Rothenflug R., 1985, A&AS, 60, 425
Arnaud M., Raymond J., 1992, ApJ, 398, 394
Asplund M., Grevesse N., Sauval A. J., astro-ph/0410214
Bell K. L., Gilbody H. B., Hughes J. G., Kingston A. E., Smith F. J., 1983, J. Phys. Chem. Ref. Data., 12, 891
Blum R. D., Pradhan A. K., 1992, ApJS, 80, 425
Bodaghee A., Santos N. C., Israelian G., Mayor M., 2003, A&A, 404, 715
Burgess A., 1964, ApJ, 139, 776
Burgess A., 1965, in E.H. Avrett, O.J. Gingerich, & C.A. Whitney eds., in proc. Second Harvard-Smithsonian Conference on Stellar Atmospheres, SAO Special Report No. 167, Smithsonian Institution Astrophysical Observatory, p.47
Burton W. M., Jordan C., Ridgeley A., Wilson R., 1971, Phil. Trans. Roy. Soc., London, A270, 81
Burton W. M., Jordan C., Ridgeley A., Wilson R., 1973, A&A, 27, 101
Cardelli J. A., Meyer D. M., Jura M., Savage B. D., 1996, ApJ, 467, 334
Carlsson M., 1986, Uppsala Astronomical Observatory, Report No. 33
Crawford H. J., Price P. B., Sullivan J. D., 1972, ApJL, 175, L149
Cunto W., Mendoza C., Ochsenbein F., Zeippen C. J., 1993, A&A, 275, L5
Cuntz M., Rammacher W., Ulmschneider P., Musielak Z. E., Saar S. H., 1999, ApJ, 552, 1053
Dere K. P., Landi E., Young P. R., Del Zanna G., 2001, ApJS, 134, 331
Dere K. P., Landi E., Mason H. E., Monsignori Fossi B. C., Young P. R., 1997, A&AS, 125, 149
Drake J. J., Smith G., 1993, ApJ, 412, 797
Drake J. J., Laming J. M., Widing K. G., 1995, ApJ, 443, 393
Drake J. J., Laming J. M., Widing K. G., 1997, ApJ, 478, 403
Dring A. R., Linsky J., Murthy J., Henry R. C., Moos W., Vidal-Madjar A., Audouze J., Landsman W., 1997, ApJ, 488, 760
Dufton P. L., Kingston A. E., 1991, MNRAS, 248, 827
Dupree A. K., 1972, ApJ, 178, 527
Feldman U., Mandelbaum P., Seely J. F., Doschek G. A., Gursky H., 1992, ApJS, 81, 387
Fontenla J. M., Avrett E. H., Loeser R., 1993, ApJ, 406, 319
Fontenla J. M., Avrett E. H., Loeser R., 2002, ApJ, 572, 636
Goldberb L., Dupree A. K., Allen J. W., 1965, Annales d'Astrophysique, 28, 589
Grevesse N., Sauval A. J., 1998, Space Sci. Rev., 85, 161
Griesmann U., Kling R., 2000, ApJL, 536, L113
Griffiths N. W., Jordan C., 1998, ApJ, 497, 883
Harper G. M., 1992, MNRAS, 256, 37
Hubeny I., Lites B. W., 1995, ApJ, 455, 376
Jordan C., 1969a, MNRAS, 142, 501
Jordan C., 1969b, ApJ, 156, 49
Jordan C., Brown A., 1981 in R. M. Bonnet & A. K. Dupree eds., Solar Phenomena in Stars and Stellar Systems, NATO ASIC, 68, Reidel. Dordrecht, Holland, p.199
Jordan C., Macpherson K. P., Smith G. R., 2001, MNRAS 328, 1098
Jordan C., Smith G. R., Houdebine E. R., 2005, MNRAS submitted
Jordan C., McMurry A. D., Sim S. A., Arulvel M., 2001b, MNRAS, 322, L5
Jordan C., Sim S. A., McMurry A. D., Arulvel M., 2001a MNRAS, 326, 303
Jordan C., Ayres T. R., Brown A., Linsky J. L., Simon T., 1987, MNRAS, 225, 903
Jordan C., Doschek G. A., Drake, J. J., Galvin A. B., Raymond J. C., 1998, in R. A. Donahue & J. A. Bookbinder eds., ASP Conf. Ser. 154: Cool Stars, Stellar Systems, and the Sun, 10, p. 91
Judge P. G., Brekke P., 1994, in eds. K. S. Balasubramaniam & G. Simon, Proc. 14th International Summer Workshop: Solar Active Region Evolution – Comparing Models with Observations, San Francisco: ASP, p. 321
Judge P. G., Carlsson M., Stein R. F., 2003, ApJ, 597, 1158
Judge P. G., Hubeny V., Brown J. C., 1997, ApJ, 475, 275
Judge P. G., Woods T. N., Brekke P., Rottman G. J. 1995, ApJ, 455, L85
Kaufman V., Martin W. C., 1993, J. Phys. Chem. Ref. Data, 22 279
Kelch W. L., 1978, ApJ, 222, 931
Kurucz R. L., Bell B., 1995, Atomic Line Data CD-ROM No. 23, Cambridge, Mass: S. A. O.

Laming J. M., Drake J. J., 1999, ApJ, 516, 324
Laming J. M., Drake J. J., Widing K. G., 1995, ApJ, 443, 416
Laming J. M., Drake J. J., Widing K. G., 1996, ApJ, 462, 948
McIntosh S. W., Brown J. C., Judge P. G., 1998, A&A, 333, 333
McMurry A. D., Jordan C., 2000, MNRAS, 313, 423
Mazzotta P., Mazzitelli G., Colafrancesco S., Vittorio N., 1998, A&AS, 133,403
Nahar S. N., 1995, ApJS, 101, 423
Nahar S. N., 1996, ApJS, 106, 213
Nahar S. N., 1999, ApJS, 120, 131
Nahar S. N. Pradhan A. K., 1997, ApJS, 111, 339
Nahar S. N., Pradhan A. K., Zhang H. L., 1995, ApJS, 131, 375
Pietarila A., Judge P. G., 2004, ApJ, 606, 1239
Redfield S., Linsky J. L., 2002, ApJS, 139, 439
Redfield S., Linsky J. L., Ake T. B., Ayres T. R., Dupree A. K., Robinson R. D., Wood B. E., Young P. R., 2002, ApJ, 581, 626
Sankrit R., Kruk J. W., Ake T. B., Andersson B.-G., 2001, FUSE Data Analysis Cookbook, Version 1.0
Scharmer G. B., Carlsson M., 1985a, J. Comput. Phys., 59, 56
Scharmer G. B., Carlsson M., 1985b, in J. Beckman & L. Crivellari eds., Progress in Stellar Spectral Line Formation Theory, NATO ASI Series C, 152, p. 189
Shine R. A., 1983, ApJ, 266, 882
Simon T., Kelch W. L., Linsky J. L., 1980, ApJ, 237, 72
Sim S. A., 2001, MNRAS, 326, 821
Sim S. A., 2002, D.Phil Thesis, University of Oxford
Sim S. A., Jordan C., 2003a, MNRAS, 341, 517
Sim S. A., Jordan C., 2003b, MNRAS, 346, 846
Summers H. P., 1972, MNRAS, 158, 255
Summers H. P., 1974a, MNRAS, 169, 663
Summers H. P., 1974b, Culham Lab. Tech. Rep., 367
Thatcher J. D., Robinson R. D., Rees D. E., 1991, MNRAS, 250, 14
Uitenbroek H., 1989, A&A, 213, 360
Uitenbroek H., 2001, ApJ, 557, 389
Vernazza J. E., Avrett E. H., Loeser R., 1973, ApJ, 184, 605
Vernazza J. E., Avrett E. H., Loeser R., 1976, ApJS, 30, 1
Vernazza J. E., Avrett E. H., Loeser R., 1981, ApJS, 45, 635
Wood B. E., Ambruster C. W., Brown A., Linsky J. L., ApJ, 542, 411
Zhao G., Chen Y. Q., Qiu H. M., Li Z. W., 2002, ApJ, 124, 2224

A1. Logarithmic ionization fractions computed for C (see Section 3).

$\log T_e$(K)	Ionization fraction		
	C II	C III	C IV
4.00	-1.45	–	–
4.10	-0.34	–	–
4.20	-0.04	-4.05	–
4.30	-0.01	-2.41	–
4.40	-0.03	-1.20	–
4.50	-0.18	-0.48	-4.72
4.60	-0.52	-0.16	-3.00
4.70	-0.97	-0.06	-1.74
4.80	-1.46	-0.09	-0.83
4.90	-2.07	-0.32	-0.31
5.00	-2.97	-0.89	-0.24
5.10	-4.08	-1.75	-0.62
5.20	-5.29	-2.72	-1.21
5.30	-6.41	-3.60	-1.76
5.40	-7.33	-4.32	-2.22
5.50	–	-4.89	-2.56

APPENDIX A

Tables A1 – A4 give the computed logarithmic ionization fractions for C, N O and Si, respectively. See Section 3 for details of these calculation.

APPENDIX B

Tables B1 – B3 give parameters for the atmospheric models A, B and C (as presented in Sections 5 and 6, respectively).

A2 Logarithmic ionization fractions computed for N (see Section 3).

$\log T_e$(K)	Ionization fraction		
	N III	N IV	N V
4.60	-0.54	-3.88	–
4.70	-0.18	-2.33	–
4.80	-0.09	-1.29	-4.55
4.90	-0.15	-0.59	-2.69
5.00	-0.42	-0.25	-1.41
5.10	-0.89	-0.21	-0.60
5.20	-1.61	-0.52	-0.30
5.30	-2.65	-1.19	-0.50
5.40	-3.79	-2.03	-0.97
5.50	-4.85	-2.85	-1.48

A3 Logarithmic ionization fractions computed for O (see Section 3).

$\log T_e$(K)	Ionization fraction			
	O III	O IV	O V	O VI
4.50	-1.83	–	–	–
4.60	-0.77	-4.64	–	–
4.70	-0.24	-2.74	–	–
4.80	-0.09	-1.53	-5.27	–
4.90	-0.11	-0.77	-3.37	–
5.00	-0.30	-0.32	-1.99	–
5.10	-0.66	-0.16	-1.06	-3.25
5.20	-1.16	-0.23	-0.49	-1.76
5.30	-1.80	-0.53	-0.28	-0.81
5.40	-2.66	-1.11	-0.44	-0.41
5.50	-3.84	-2.04	-1.03	-0.55

A4 Logarithmic ionization fractions computed for Si (see Section 3).

$\log T_e$(K)	Ionization fraction		
	Si II	Si III	Si IV
4.00	-0.01	-1.74	–
4.10	-0.03	-1.18	–
4.20	-0.09	-0.71	–
4.30	-0.33	-0.27	-4.23
4.40	-0.94	-0.05	-2.67
4.50	-1.60	-0.04	-1.27
4.60	-2.10	-0.18	-0.49
4.70	-2.53	-0.39	-0.24
4.80	-3.06	-0.69	-0.20
4.90	-3.92	-1.33	-0.53
5.00	-5.14	-2.36	-1.15
5.10	-6.28	-3.30	-1.67
5.20	-7.21	-4.02	-2.03
5.30	-8.16	-4.77	-2.48
5.40	–	-4.86	-2.93
5.50	–	-5.65	-3.45

B1 Model A. m_{col} is the column mass density, T_e is the electron temperature, N_e is the electron number density, N_H is the hydrogen number density and $\xi_{\rm micro}$ is the most-probable microturbulent velocity.

$\log m_{col}$ g cm^{-2}	$\log T_e$ K	$\log N_e$ cm^{-3}	$\log N_H$ cm^{-3}	$\xi_{\rm micro}$ km s^{-1}
-4.50798	5.490	10.31	10.23	20.95
-4.50786	5.410	10.38	10.30	20.95
-4.50777	5.331	10.46	10.38	20.95
-4.50769	5.250	10.53	10.45	20.95
-4.50761	5.170	10.60	10.53	20.95
-4.50754	5.091	10.68	10.60	20.95
-4.50747	5.010	10.75	10.67	20.95
-4.50740	4.930	10.81	10.73	20.95
-4.50737	4.890	10.85	10.77	20.84
-4.50734	4.849	10.88	10.81	20.40
-4.50730	4.810	10.92	10.84	19.98
-4.50727	4.769	10.96	10.88	19.54
-4.50723	4.731	10.99	10.91	19.13
-4.50719	4.689	11.03	10.95	18.69
-4.50714	4.650	11.06	10.99	18.27
-4.50708	4.610	11.10	11.02	17.84
-4.50701	4.570	11.14	11.06	17.41
-4.50693	4.530	11.17	11.09	16.98
-4.50682	4.490	11.21	11.13	16.56
-4.50670	4.450	11.24	11.17	16.12
-4.50655	4.410	11.27	11.21	15.70
-4.50636	4.370	11.29	11.25	15.27
-4.50613	4.330	11.32	11.29	14.84
-4.50585	4.290	11.35	11.33	14.41
-4.50550	4.250	11.37	11.37	13.98
-4.50507	4.210	11.39	11.41	13.55
-4.50453	4.170	11.42	11.46	13.12
-4.50381	4.130	11.44	11.50	12.70
-4.50278	4.090	11.45	11.55	12.27
-4.50116	4.050	11.44	11.60	11.84
-4.49819	4.010	11.43	11.66	11.41
-4.49184	3.970	11.41	11.72	10.98
-4.47421	3.930	11.34	11.80	10.55
-4.40442	3.890	11.18	11.93	10.12
-4.15000	3.855	11.04	12.24	9.75
-3.86000	3.835	11.02	12.56	9.53
-3.49000	3.815	11.05	12.95	9.32
-3.13000	3.785	11.02	13.39	8.01
-2.80000	3.748	10.89	13.83	6.27
-2.41000	3.712	10.81	14.32	4.76
-2.06000	3.678	10.85	14.76	3.41
-1.80000	3.651	11.03	15.08	2.40
-1.69000	3.639	11.12	15.21	1.97
-1.57000	3.626	11.21	15.35	1.56
-1.43000	3.619	11.31	15.51	1.31
-1.27000	3.617	11.43	15.67	1.25
-1.06000	3.618	11.59	15.88	1.25
-0.86000	3.619	11.74	16.08	1.25
-0.61000	3.619	11.92	16.33	1.25
-0.39000	3.619	12.08	16.54	1.25
-0.15000	3.621	12.25	16.78	1.25
0.06000	3.626	12.43	16.99	1.25
0.26000	3.641	12.66	17.17	1.25
0.43000	3.666	12.93	17.32	1.25
0.59893	3.704	13.24	17.45	1.25
0.70717	3.736	13.44	17.53	1.25
0.79292	3.763	13.65	17.59	1.25
0.87069	3.788	13.91	17.64	1.25

B2 Model B. m_{col} is the column mass density, T_e is the electron temperature, N_e is the electron number density, N_H is the hydrogen number density and $\xi_{\rm micro}$ is the most-probable microturbulent velocity.

$\log m_{col}$ g cm^{-2}	$\log T_e$ K	$\log N_e$ cm^{-3}	$\log N_H$ cm^{-3}	$\xi_{\rm micro}$ km s^{-1}
-4.50517	5.490	10.31	10.25	19.15
-4.50505	5.410	10.39	10.32	19.15
-4.50494	5.330	10.46	10.40	19.15
-4.50483	5.250	10.54	10.47	19.15
-4.50472	5.169	10.61	10.55	19.15
-4.50463	5.089	10.69	10.62	19.15
-4.50455	5.009	10.76	10.69	19.15
-4.50450	4.949	10.81	10.75	19.15
-4.50446	4.910	10.84	10.78	19.15
-4.50443	4.871	10.88	10.82	18.80
-4.50439	4.829	10.92	10.85	18.31
-4.50436	4.790	10.96	10.89	17.85
-4.50432	4.750	10.99	10.93	17.37
-4.50429	4.710	11.03	10.97	16.90
-4.50425	4.671	11.07	11.00	16.42
-4.50420	4.630	11.11	11.04	15.93
-4.50414	4.590	11.14	11.08	15.44
-4.50406	4.550	11.18	11.12	14.95
-4.50397	4.510	11.22	11.15	14.46
-4.50386	4.470	11.26	11.19	13.96
-4.50373	4.430	11.29	11.24	13.45
-4.50358	4.390	11.32	11.28	12.94
-4.50345	4.350	11.35	11.33	12.42
-4.50330	4.310	11.38	11.37	11.90
-4.50311	4.270	11.42	11.41	11.37
-4.50282	4.230	11.45	11.46	10.83
-4.50238	4.190	11.48	11.51	10.28
-4.50164	4.150	11.51	11.56	9.72
-4.50037	4.110	11.54	11.61	9.14
-4.49767	4.070	11.57	11.67	8.55
-4.49026	4.030	11.59	11.73	7.93
-4.47013	3.990	11.60	11.83	7.29
-4.43521	3.950	11.55	11.95	6.61
-4.37097	3.910	11.45	12.11	5.89
-4.20254	3.870	11.29	12.38	5.10
-3.90000	3.838	11.19	12.75	4.40
-3.60000	3.813	11.14	13.09	3.78
-3.25000	3.785	11.08	13.48	3.31
-2.99000	3.764	11.02	13.77	3.01
-2.61000	3.731	10.92	14.20	2.56
-2.22000	3.694	10.87	14.63	2.10
-2.06000	3.678	10.90	14.81	1.91
-1.92000	3.664	10.97	14.97	1.74
-1.80000	3.651	11.06	15.11	1.60
-1.69000	3.639	11.14	15.23	1.47
-1.57000	3.626	11.22	15.37	1.34
-1.43000	3.619	11.31	15.51	1.27
-1.27000	3.617	11.43	15.68	1.25
-1.06000	3.618	11.60	15.89	1.25
-0.86000	3.619	11.75	16.08	1.25
-0.61000	3.619	11.93	16.33	1.25
-0.39000	3.619	12.08	16.55	1.25
-0.15000	3.621	12.26	16.79	1.25
0.06000	3.626	12.43	16.99	1.25
0.26000	3.641	12.66	17.18	1.25
0.43000	3.666	12.93	17.33	1.25
0.59893	3.704	13.24	17.46	1.25
0.70717	3.736	13.45	17.54	1.25
0.79292	3.763	13.66	17.60	1.25
0.87069	3.788	13.92	17.65	1.25

B3 Model C. m_{col} is the column mass density, T_e is the electron temperature, N_e is the electron number density, N_H is the hydrogen number density and $\xi_{\rm micro}$ is the most-probable microturbulent velocity.

$\log m_{col}$ g cm^{-2}	$\log T_e$ K	$\log N_e$ cm^{-3}	$\log N_H$ cm^{-3}	$\xi_{\rm micro}$ km s^{-1}
-4.54760	5.490	10.27	10.20	19.15
-4.54746	5.410	10.34	10.28	19.15
-4.54732	5.330	10.42	10.36	19.15
-4.54719	5.250	10.50	10.43	19.15
-4.54706	5.171	10.57	10.50	19.15
-4.54695	5.090	10.64	10.58	19.15
-4.54685	5.011	10.71	10.65	19.15
-4.54676	4.930	10.79	10.72	19.15
-4.54668	4.850	10.86	10.79	18.55
-4.54660	4.770	10.93	10.87	17.61
-4.54652	4.689	11.01	10.94	16.64
-4.54648	4.649	11.05	10.98	16.16
-4.54644	4.611	11.08	11.02	15.70
-4.54640	4.570	11.12	11.05	15.20
-4.54636	4.530	11.16	11.09	14.71
-4.54632	4.489	11.20	11.13	14.20
-4.54627	4.450	11.23	11.17	13.71
-4.54622	4.411	11.26	11.21	13.20
-4.54614	4.370	11.29	11.26	12.69
-4.54604	4.330	11.32	11.30	12.17
-4.54591	4.290	11.35	11.35	11.64
-4.54573	4.250	11.38	11.40	11.10
-4.54543	4.210	11.41	11.45	10.56
-4.54492	4.170	11.43	11.50	10.00
-4.54408	4.130	11.46	11.55	9.43
-4.54267	4.090	11.48	11.61	8.85
-4.54026	4.050	11.48	11.68	8.24
-4.53602	4.010	11.48	11.75	7.61
-4.52840	3.970	11.45	11.83	6.95
-4.51317	3.930	11.38	11.93	6.26
-4.45968	3.890	11.24	12.07	5.50
-4.38000	3.870	11.13	12.20	5.09
-4.26000	3.854	11.05	12.35	4.75
-4.07000	3.838	11.00	12.58	4.39
-3.85907	3.824	10.99	12.81	4.06
-3.54154	3.806	11.00	13.16	3.63
-3.21000	3.782	10.98	13.53	3.27
-2.90422	3.757	10.94	13.87	2.90
-2.57000	3.727	10.91	14.24	2.51
-2.45000	3.716	10.91	14.38	2.37
-2.22000	3.694	10.98	14.63	2.10
-2.06000	3.678	11.09	14.81	1.91
-1.92000	3.664	11.20	14.97	1.74
-1.80000	3.651	11.30	15.11	1.60
-1.69000	3.639	11.37	15.23	1.47
-1.57000	3.626	11.44	15.37	1.34
-1.43000	3.619	11.52	15.51	1.27
-1.27000	3.617	11.63	15.68	1.25
-1.06000	3.618	11.78	15.89	1.25
-0.86000	3.619	11.93	16.08	1.25
-0.61000	3.619	12.10	16.33	1.25
-0.39000	3.619	12.25	16.55	1.25
-0.15000	3.621	12.42	16.79	1.25
0.06000	3.626	12.59	16.99	1.25
0.26000	3.641	12.82	17.18	1.25
0.43000	3.666	13.11	17.33	1.25
0.59893	3.704	13.44	17.46	1.25
0.70717	3.736	13.64	17.54	1.25
0.79292	3.763	13.82	17.60	1.25
0.87069	3.788	14.02	17.65	1.25